



Invited Review

## Fabric and anisotropy of slates: From classical studies to new results



H.-R. Wenk<sup>a,\*</sup>, R. Yu<sup>a,b</sup>, V. Cárdenes<sup>c</sup>, M.A. Lopez-Sánchez<sup>d</sup>, M. Sintubin<sup>e</sup>

<sup>a</sup> Department of Earth and Planetary Science, University of California, Berkeley, 94720, CA, USA

<sup>b</sup> Xi'an Polytechnic University, Xi'an, China

<sup>c</sup> Department of Geology, Oviedo University, 33005, Oviedo, Spain

<sup>d</sup> Géosciences Montpellier, Université de Montpellier & CNRS, Place E. Bataillon, Montpellier, 34095, cedex 5, France

<sup>e</sup> Department of Earth and Environmental Sciences, KU Leuven, B-3001, Leuven, Belgium

A B S T R A C T

Slates are low-grade metamorphic argillaceous rocks which have developed an intense tectonic fabric, referred to as slaty cleavage. Due to their unique properties they have long been used as building materials, especially tiles for roofs and floors. The fabric, characterized by strong alignment of platy phyllosilicate crystals, produces extreme anisotropy that has been of great interest in structural geology: What different fabric types are observed? How do they form? Here we review crystal preferred orientation (CPO) and add new information to establish a comprehensive base for future studies. Slates are composed of fine-grained phyllosilicates (dominantly white mica and chlorite, sometimes chloritoid), quartz and accessories. Texture analyses of these polyphase rocks with high energy synchrotron X-ray diffraction and high resolution EBSD reveal strong alignment of mica and chlorite, in some cases exceeding any previously reported texture strength, including metals. Interestingly, the CPO of quartz, with highly flattened grains (shape preferred orientation or SPO), is practically random. Recrystallization microstructures observed by scanning electron microscopy suggest that the phyllosilicate preferred orientation is largely caused by crystal growth under stress, and that quartz was subject to pressure solution and reprecipitation, producing an anisotropic shape. While phyllosilicates preferred orientation in slates is much higher than reports for shale, schists and gneiss, elastic seismic anisotropy for slates is similar to shales where a significant component is due to aligned porosity.

### 1. Introduction

Slates are extraordinary metamorphic rocks characterized by their unique fabric and strength. They have been a focus in structural geology (e.g. Passchier and Trouw, 2005; Twiss and Moores, 2006; Marshak, 2016; Fossen, 2016) as well as engineering (e.g. Cárdenes et al., 2014; Wickert, 2020). There are no other rocks that cleave over large planar surfaces at the millimeter scale. Because of the strength, thermal stability and chemical inertness, slates have been widely used as roof and floor tiles, as well as school boards (e.g. Richards, 2007).

The excellent cleavage properties and the large anisotropy of elastic properties (e.g. Christensen, 1965) are clearly correlated with the alignment of phyllosilicates such as muscovite and chlorite. A previous review focused on industrial slate production (Cárdenes et al., 2014). Here we emphasize microstructures and preferred orientation, both of crystals (CPO) and grain shapes (SPO), as well as elastic anisotropy. First we give a brief summary about the geologic occurrence of slates and their origin and tectonic significance. Then we discuss slate production, from ancient Rome to modern times.

Because of the unique properties there have been early studies to investigate microstructures characterizing slate, first with optical

microscopy in the 19th century (e.g. Sorby, 1853, 1856) and later with scanning electron microscopy (SEM) and transmission electron microscopy (TEM) (e.g. Oertel and Phakey, 1972; Oertel et al., 1973; Knipe and White, 1977; White and Knipe, 1978). Since these rocks are very fine-grained, optical microscopy with a universal stage first introduced for texture analysis by Schmidt (1925) cannot be applied to quantify preferred orientation. Early also X-ray diffraction has been used (Sander and Sachs, 1930). Later X-ray pole figure goniometry was applied (e.g. Oertel and Phakey, 1972). More recently advanced methods such as synchrotron X-ray diffraction revealed unique alignment of mica in slates from the Belgian Ardennes, with stronger alignment than recrystallized metal sheets (Wenk et al., 2019). This stimulated this project to revisit classical studies of slate CPO and discuss it in a broader context by comparing results from older methods with investigations of a range of slates from different environments with new techniques, to provide a basis for better understanding slate anisotropy. Results confirm that the intense alignment of the slate from the Ardennes is not unique but advanced methods and data analysis are required to document this exceptional preferred orientation.

In the discussion we review the significance of phyllosilicate content on anisotropy, mechanisms that may be responsible for creating the

\* Corresponding author.

E-mail address: [wenk@berkeley.edu](mailto:wenk@berkeley.edu) (H.-R. Wenk).

orientation patterns, compare fabric features of slates with shales and gneiss, and explain how CPO can be used to predict elastic anisotropy. Focus in this review is on CPO, not on the tectonic history or metamorphic conditions that produced these rocks. While this is a review, we hope we can stimulate other researchers to follow up with future systematic studies of slate preferred orientation, particularly from well-defined environments, applying high energy synchrotron X-ray diffraction and electron back-scatter diffraction (EBSD). Many issues remain unresolved.

## 2. Geological background of slate deposits

Slates are argillaceous rocks composed mainly of muscovite, chlorite and quartz. They transformed during relatively low-grade metamorphism from sedimentary shales during tectonic events. Slates display an extraordinary cleavage with perfectly planar surfaces as observed for example in Mort Slate at Bull Point, North Devon (UK) (Fig. 1). The transformation of shales to slates occurs dominantly at greenschist facies metamorphism.

Slates occur worldwide and span a wide range of ages, ranging from Paleoproterozoic in Hebei, China (e.g. Xue, 2002; Jinbiao, 2010), Cambrian (e.g. Newfoundland, Canada, e.g. Alam et al., 2008; Argentina, e.g. Chernicoff et al., 2008; Wales, U.K. such as Penrhyn, e.g. Attewell and Taylor, 1969; Gwyn, 2015; Hughes et al., 2016), Ordovician (e.g. Ratcliffe et al., 2011; Cárdenes et al., 2014), Devonian (e.g. Ardennes, Belgium and France, e.g. Voisin, 1987; Sintubin, 1996; Hunsrück, Germany e.g. Wagner et al., 1997), to upper Cretaceous (Liguria, Italy, e.g. Brandolini, 1988; Del Soldato and Coli, 2013). The extraordinary cleavage in slates has been of long-standing interest (e.g. Sorby, 1853, 1856; Dieterich, 1969; Siddans, 1972; Wood, 1974; Means, 1981; Weber, 1981). Cleavage is the property of rocks to break along planar structures and, in the case of slates, schists and gneiss it is related to the preferred orientation of phyllosilicates with a planar morphology (Ramsay and Huber, 1983). Publications in structural geology discuss how cleavage in slates develops during low-grade metamorphism from shales (e.g. Tullis, 1976; Wood and Oertel, 1980; Lee et al., 1986; Ishii, 1988; Merriman et al., 1990; Ho et al., 2001).

In shales cleavage is parallel to the bedding plane formed during sedimentation and compaction. During the transformation of shales to slates the sedimentary bedding plane is sometimes preserved. However, often the slaty cleavage deviates significantly from the bedding plane as in a sample of slate from the Valdeorras in Northern Spain (Fig. 2). The cleavage with perfectly planar surfaces may extend over many meters (Fig. 3). But slate deposits are often heterogeneous due to compositional variations and folding as illustrated for a quarry in Valdeorras (Fig. 4).

The slaty cleavage is a secondary, tectonic fabric developing in low-grade metamorphic conditions in argillaceous rocks. It reflects the finite strain that the argillaceous rock has undergone (see Siddans, 1972; Wood, 1974; for overviews). The slaty cleavage primarily represents a flattening strain, caused by the phyllosilicates preferred orientation, with the platelets



Fig. 1. Slate outcrops Bull Point, N Devon, UK (courtesy Martin Fowler).



Fig. 2. Section looking along the cleavage plane (horizontal) of slate from Valdeorras, N Spain, with the bedding plane inclined.



Fig. 3. Slate quarry in Jiangxi (China) with perfectly planar cleavage surfaces. oriented perpendicular to the principal shortening direction. Slaty cleavage development is often associated with folding and develops parallel to the axial plane of the folds.

In hand specimens slaty cleavage can be very homogeneous with no other microscopic fabric features (Fig. 5a). However, often the fabric is more complex with domainal fabrics (e.g. Powell, 1979). Due to the highly planar fabric at the micron scale, multiple strain episodes can lead to kinking and microfolds (Fig. 5b). Sometimes two cleavages are present and the slate displays a pencil-like morphology (Fig. 5c). Within the cleavage plane, a stretching lineation may develop parallel to the extension direction (Fig. 5d). In this example from Hunsrück, Germany, the cleavage coincides with the original bedding plane, illustrated by a fossil (*Aspidosoma tischbeinianum*). Besides the stretching lineation, different types of intersection lineations can often be recognized on cleavage planes. The most common one is the bedding-cleavage intersection lineation, often parallel to the fold hinge line of associated folds (e.g. Fig. 2). Another type of intersection lineation is caused by the development of a secondary tectonic fabric, resulting in a crenulation of the primary cleavage fabric (Fig. 5e).

Slate belts occupy a specific position in an orogenic system, in between the non-metamorphosed, foreland fold-and-thrust belt and the higher-grade, crystalline internal domains of the orogeny. They accommodate



**Fig. 4.** Slate outcrop in one of the Valdeorras quarries (N Spain), illustrating the compositional and structural heterogeneities with high quality slates restricted to local areas.

significant shortening (up to 60%) and drive the development of the foreland fold-and-thrust belt (e.g. Le Gall, 1992). Paleo-geographically slate belts represent the vestiges of rapid synrift of sedimentary basin fills, preceding a rift-drift transition, and leaving behind the aborted rift basins on the passive continental margins (e.g. Onccken et al., 2000).

### 3. Slate as building material

Slate is a classic building material in European historic and modern architecture (Fig. 6). In 2018, the volume of slate traded on the World market was over 10 million tons, valued at over 12 billion US\$. Of this, roofing slate represents about 10% in volume and 5% in value of World trade (data: United Nations Statistics Division UNSTATS, statistical



**Fig. 6.** View of the town of Matrelange in Wallonia (Belgium) with slates used on roofs and walls of historic buildings.

codes 6802 for natural building stone, i.e. marble, granite, etc., and 6803 for roofing slate).

The main characteristic of slate, the slaty cleavage, is most significant from a construction standpoint. Slate is easy to split into regular blocks with many applications. However, not all slates have the high degree of homogeneity needed to produce roofing slate shingles, 4 or 8 mm in thickness and 20 × 30 cm in size. Several types of metamorphic rocks are used as roofing slates, but the commonest lithologies (together with their estimated production volume) are low grade slate (5%) – slate (92%) – phyllite (1.5%) – mica schist (1.5%). Roofing slate is classified using two parameters: color and petrology. Color is the result of the environmental genetic conditions, which determine the occurrence of small quantities of coloring minerals (black: organic matter; green: chlorite; red: hematite), while petrology refers to both the lithology and microscopic arrangement of the rock.

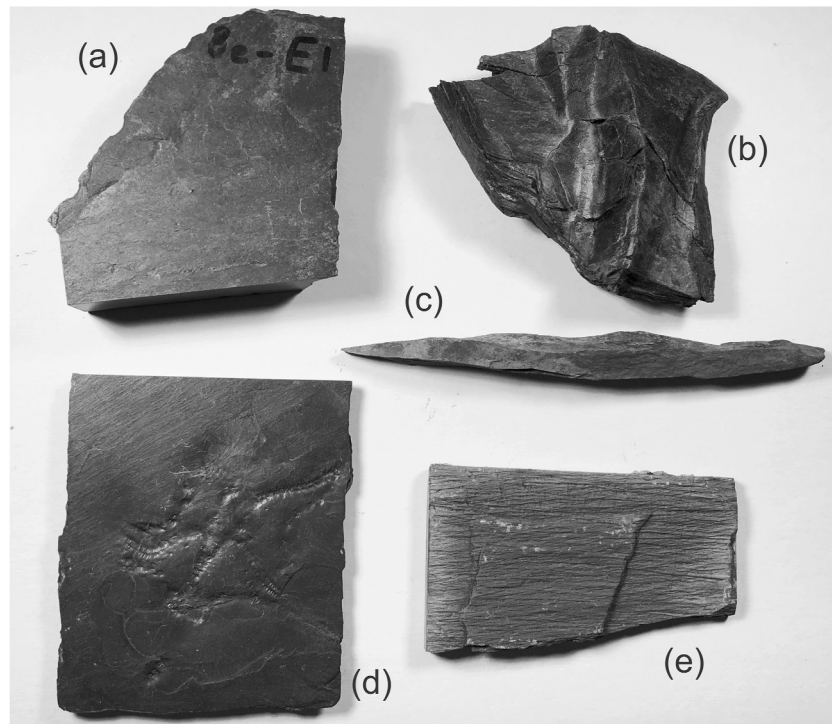


**Fig. 5.** Hand specimens displaying the morphology of slates. (a) High quality roofing slate from La Fortelle quarry, Belgium (Be-E1), (b) sample from La Fortelle with secondary deformation kinking, (c) pencil-shaped slate from Ruhrsee with two cleavages (Be-A), (d) slate from Hunsrück, Germany with fossil *Aspidosoma tischbeinianum*; here the cleavage is parallel to the bedding plane (Sturtz85), (e) Slate with crenulation from China (Ch1).



**Fig. 7.** Historic roofing slate shingle, Bronze age from Castro da Cidade, Spain.

Slate architecture has evolved together with the development of the manufacturing process. In the Bronze age slate sheets were extracted from outcrops with little formatting, just one or two holes for wooden nails (Fig. 7). First evidences of the use of slate in construction date back to Prehistoric times. Slate is an important element in the tumuli from the Neolithic-Chalcolithic age in some parts of the Iberian Peninsula (Iglesias Ponce de León, 1995). During the Bronze and Iron ages, constructions of fortified settlements (hillforts, “castros” in Spanish) were common in many regions of Europe. Some examples of these slate hillforts, in a reasonable good state of conservation, can be found in Galicia and Asturias (Spain). The oldest recorded example of civil architecture with slate is an aristocratic residence in the region of Extremadura (Spain) from the 6th century BC (Iglesias Ponce de Leon, 2012). Other examples of architecture with slate are the thermal baths from Lugo (Spain), dating back to the 1st century AD.

During the Roman Empire slate was also an important building material. There were buildings with slate walls and pavements, but only occasionally slate was used in roofs. Roman roofing slate shingles have been recovered in places such as Wales (Lindsay, 1974; Gwyn, 2015), Leicester, England (McWhirr, 1988), Flanders, Belgium (De Clercq, 2011) and Rheinland, Germany (Wagner, 2014).

After the Romans, following civilizations continued to use slate for roofing. During the Middle Ages roofing slate was considered as an exquisite material, reserved for Kings and the Church. One of the first records regarding slate quarrying is a requirement from Bishop Licinus of Anjou (Angers, France) in the 6th century to use the slate production exclusively on religious buildings (Cnudde, 1998). Later, in 1570, an ode written by a Welsh poet mentions the historic quarry of Penrhyn, where “the bard Sion Tudor asks the Dean of Bangor for a load of slates from the Caerhir quarry” (Davies, 1878). During the 16th and 17th centuries there was important trading of roofing slate between both sides of the English Channel (Wagner et al., 1994, 1995; Jope and Dunning, 2011). The slate industry became a significant source of wealth for the areas surrounding the quarries. By 1826, the first steam engine started operating at the Easdale quarry (Scotland), and by the second half of the 19th century, all Welsh quarries were mechanized. Almost every quarry had railways to transport roofing slate crates and Welsh slate was exported to the rest of the world (Gwyn, 2015; Price and Ronck, 2019).

The first slate quarry in the USA was opened in 1734 at the Peach Bottom District in Pennsylvania (Stearns et al., 2000). During the second half of the 19th century, Welsh, Italian, Irish and Slovak immigration played a major role in the development of the roofing slate industry in Slate Valley (Vermont). Roofing slate was mainly used in areas near slate outcrops in the states of Vermont, New York and Pennsylvania, mainly for singular and monumental buildings. Slate quarries were also opened in Quebec (Canada) and San Luis (Argentina).

In the 20th century, the global slate industry was severely affected by two World Wars. In the US most of the slate production was diverted to fabricate switchboards for electrical installations. Due to its low electric

conductivity, slate was ideal for this application and the demand for this use greatly increased.

In the second half of the 20th century, the European slate market, the biggest in the world, was affected by the advancement of slate mining in NW Spain. So far, the Spanish roofing slate industry had been limited to the historical quarries from Bernardos, N Madrid. These quarries had been working since the 16th century, but their production was reserved for royal buildings and churches (Cárdenes et al., 2019). However, in the 1960s, coinciding with a period of strikes and social movements in the main French production areas (Angers), the Spanish industry skyrocketed. French and German engineers had opened quarries and brought the latest mining technologies to Spain, such as electric saws and diamond wire cutting, though the final cleaving of tiles is still done with chisel and hammer (Fig. 8). The Valdeorras region transformed to a blooming slate industry. In a few years, the center of global roofing slate industry moved to this Spanish remote region, which came to manufacture up to 90% of the World's roofing slate in 2000 (Cárdenes et al., 2014; Garcia-Guinea et al., 1997, 1998; Ward and Gómez-Fernandez, 2003).

Today, the Spanish hegemony is threatened by other countries. By the beginning of the 21st century, the rapid development of new trade routes has facilitated the export of slate products from Brazil (Chiodi, 2015), China (Xue, 2002; Jinbiao, 2010, Fig. 3) and India (Sharma et al., 2019). But the quality of these roofing slates does not always meet the requirements by clients, especially the demand from France and Germany for high quality black roofing slate. The relatively low-grade green and black slates produced in Brazil are not very suitable for roofing, while India and China are not yet able to provide a reliable supply of roofing slate of high quality. Fig. 9 is an overview of slate production in 2010 with largest producers Spain, China and Brazil. In Fig. 10 slate world production and consumption are highlighted.

#### 4. Experimental methods applied to slate fabric analysis

##### 4.1. Microstructural analysis with optical and electron microscopy

Early investigations of slate fabrics relied on optical microscopy (e.g. Sorby, 1853; Williams, 1972; Roy, 1978; Morris, 1981) but since slates



**Fig. 8.** Cleaving slate with chisel and hammer from blocks cut with diamond saw in Valdeorras in 2019.

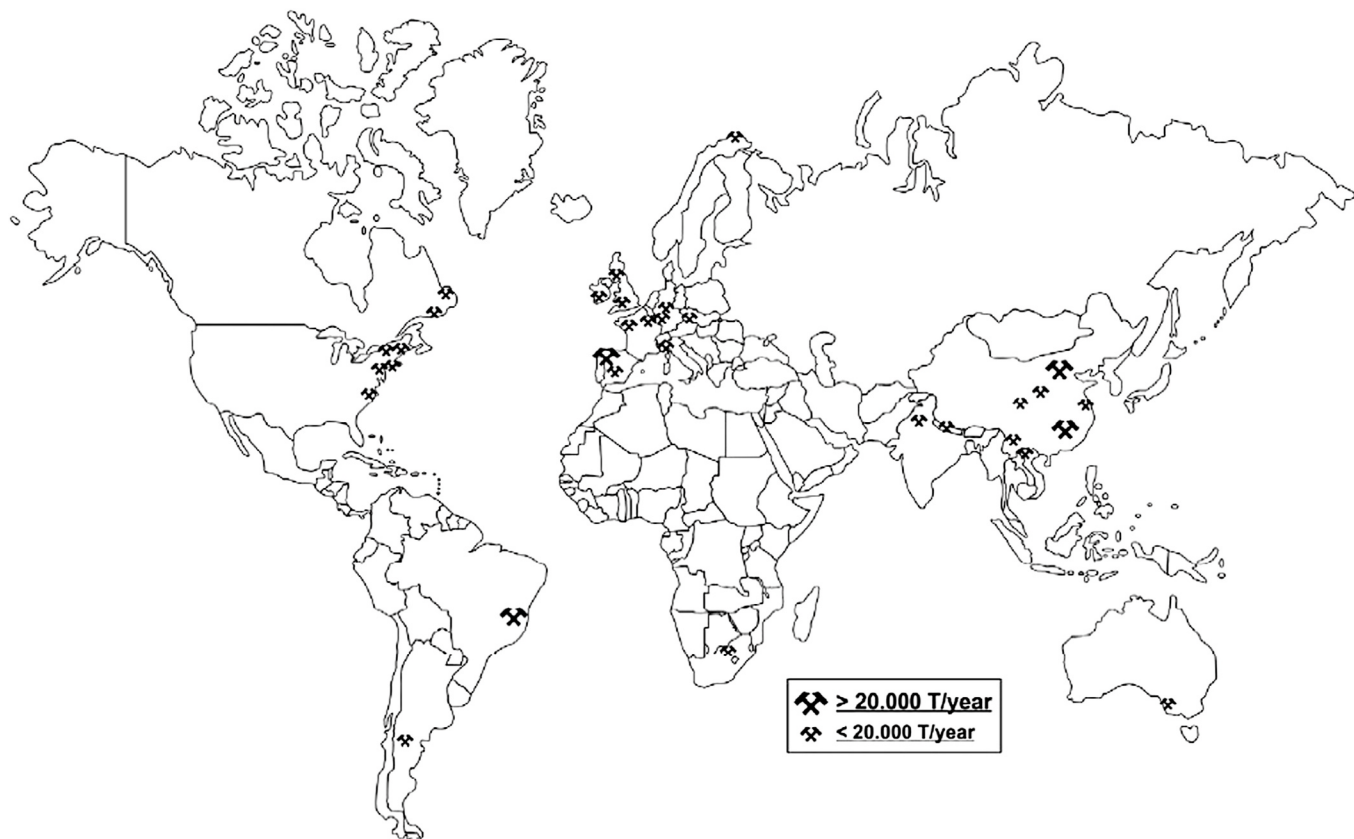


Fig. 9. Map of roofing slate production in 2010 (Cárdenes et al., 2014).

are very fine-grained, application of both scanning (SEM) and transmission electron microscopy (TEM) provided important new information to characterize and understand microstructures (e.g. Gray, 1977; Knipe and White, 1979; Knipe, 1981; Weber, 1981). With the SEM, particularly in backscatter mode (BES), mineral morphology can be visualized (examples will be discussed in section 6.2). With additional energy-dispersive detectors chemical composition can be assessed and phases can be easily identified. With electron backscatter diffraction (EBSD) crystal orientation can be mapped (see sections 4.3 and 7).

#### 4.2. Early studies using X-ray diffraction to investigate slate preferred orientation

Preferred orientation of minerals in rocks was traditionally measured in petrographic thin sections with an optical microscope equipped with a Universal Stage, enabling rotation of the thin section (e.g. Schmidt, 1925). This is not applicable to opaque materials and also to very fine-grained rocks such as slates. Here X-ray diffraction provided a new opportunity and was originally applied to metals (Wever, 1924). Sander

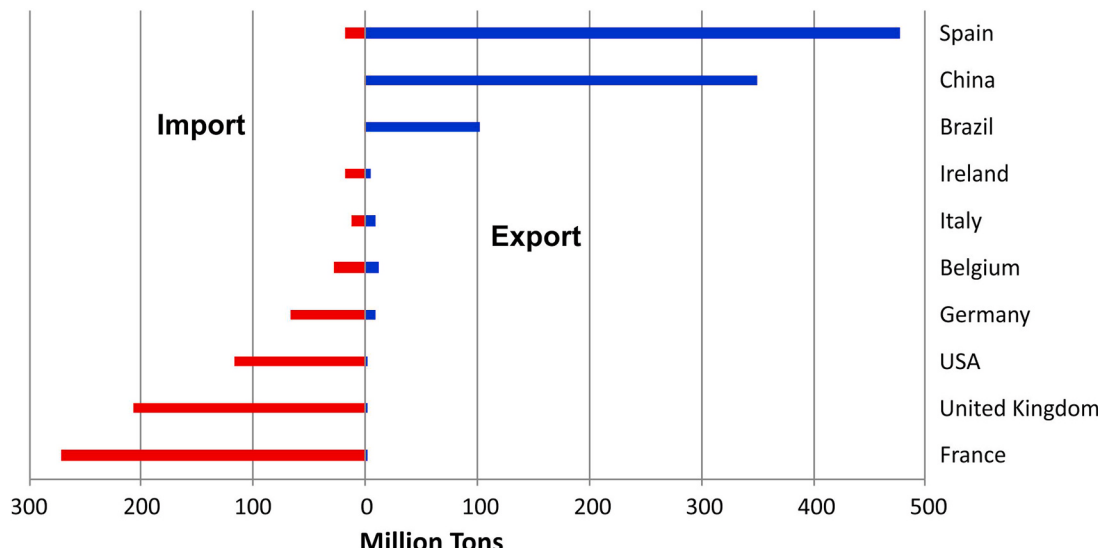
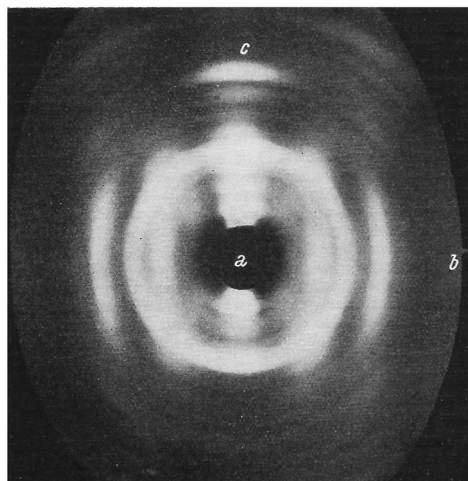


Fig. 10. Production (blue) and import (red) (Cardenes et al. 2014) of roofing slate around the World in 2010.



**Fig. 11.** Laue X-ray diffraction image of slate (Sander, 1950, his Fig. 13).

and Sachs (1930) applied the method to rocks and provided qualitative data for a Paleozoic slate from Tirol (Austria) in a photographic Laue diffraction image (Fig. 11, Sander, 1950, Fig. 13, p. 53). Subsequently photographic diffraction images were used extensively for ore minerals (Von Gehlen, 1960).

But it was only with the development of Geiger counters that quantitative X-ray texture analysis became possible (Decker et al., 1948). With a pole figure goniometer a sample is irradiated with monochromatic X-rays in reflection or transmission geometry. A detector set at the Bragg angle for a given lattice plane  $hkl$  records diffraction intensities while the sample is rotated to different orientations, covering the pole distribution of  $hkl$  relative to sample coordinates. With optical methods only quartz c-axes could be measured; with a pole figure goniometer orientations of any lattice planes could be recorded. There are complications: for example during sample tilt the irradiated area of the sample changes, peak broadening occurs and appropriate corrections need to be applied. Particularly for multiphase rocks such as slates diffraction peaks overlap and peak separation is limited. It is often difficult to accurately determine the scattering background which is very significant for strong crystal orientation patterns (some of these factors are discussed e.g. by Kocks et al., 1998,

Chapter 4). The first application of pole figure texture measurements of phyllosilicate-rich rocks was reported by Oertel (1970) and Siddans (1976) gives some details. Section 5 describes results of some of these studies.

#### 4.3. Synchrotron X-rays

Conventional X-ray tubes used for pole figure goniometry produce a broad beam ( $\sim 1$  mm) of relatively low intensity and energy (e.g. wavelength  $1.5 \text{ \AA}$  for Cu-radiation). In a synchrotron a highly focused intense beam of X-rays with monochromatic or continuous wavelengths can be produced of a wide range of energies. The use of two-dimensional digital detectors permits fast and reliable data acquisition. Fig. 12a is a schematic display of a typical experiment. The X-ray beam reaches the sample (in this case a 2-5 mm diameter cylinder mounted on an aluminum rod, Fig. 12b) and causes diffraction. The recorded image displays Debye rings and intensity variations along the rings immediately indicate the presence of texture. Fig. 13 illustrate four diffraction images of slates with different composition and fabric characteristics. In all of them there are strong intensities of basal (00l) reflections of phyllosilicates in the horizontal direction, suggesting strong alignment of (001) lattice planes perpendicular to this direction. Also all images display a more or less continuous ring for quartz 100 and 101, indicating random preferred orientation.

The use of high energy is advantageous because of good sample penetration and moderate absorption, as well as small  $2\theta$  angles. An example of a high energy beamline is 11-ID-C at the Advanced Photon Source (APS) of Argonne National Laboratory, with a monochromatic wavelength of about  $0.1 \text{ \AA}$  (energy  $\sim 115 \text{ keV}$ ) which is ten times shorter than normal laboratory X-rays. Diffraction images at this beamline are recorded within seconds with a 2D image plate detector mounted about 2 m behind the sample (Fig. 12a). During data collection the sample can be translated to obtain a representative average. A single image covers a circle on the pole figure (Fig. 12c, #1). To obtain a better coverage the sample is rotated around the axis x in increments, e.g. from  $-90^\circ$  to  $90^\circ$  in  $15^\circ$  increments of  $\omega$ .

For quantitative texture information the digital X-ray diffraction images are then analyzed with the Rietveld method (Rietveld, 1969), which relies on a least-squares fit of measured diffraction information to minimize the difference between experimental diffraction data and a calculated model based on scattering background, crystal structures,

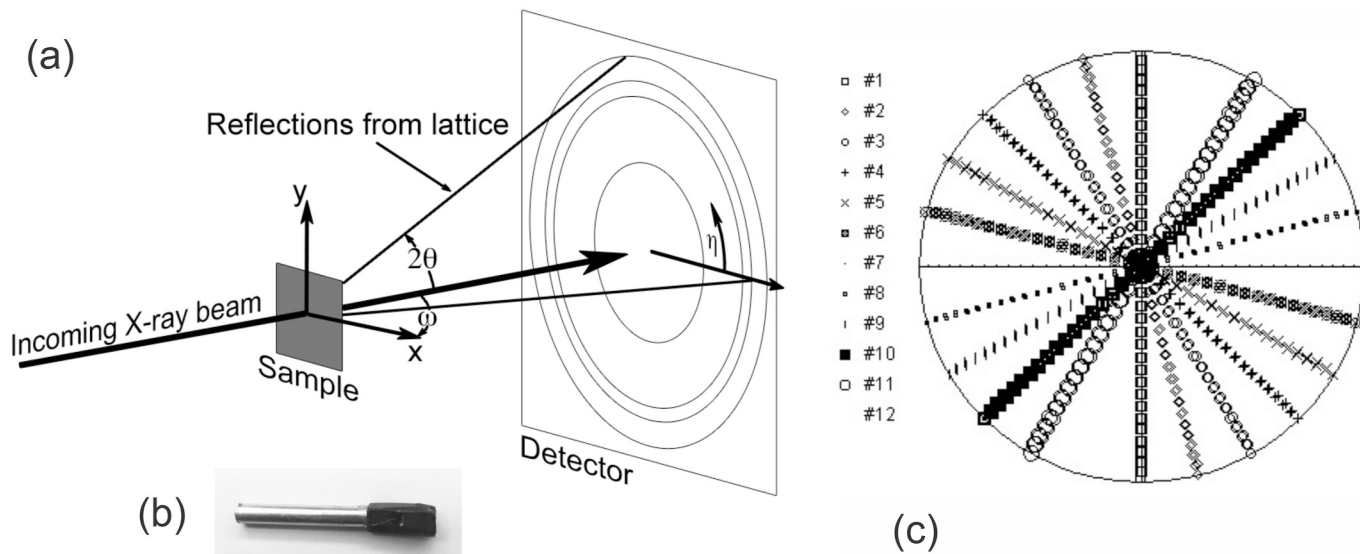


**Fig. 12.** (a) Synchrotron diffraction experiments with (b) sample morphology (aluminum rod is 5 mm in diameter), and (c) Pole figure coverage with 11 images. The sample is rotated around the axis x (perpendicular to the cleavage plane) in  $15^\circ$  increments. Equal area projection on the cleavage plane.

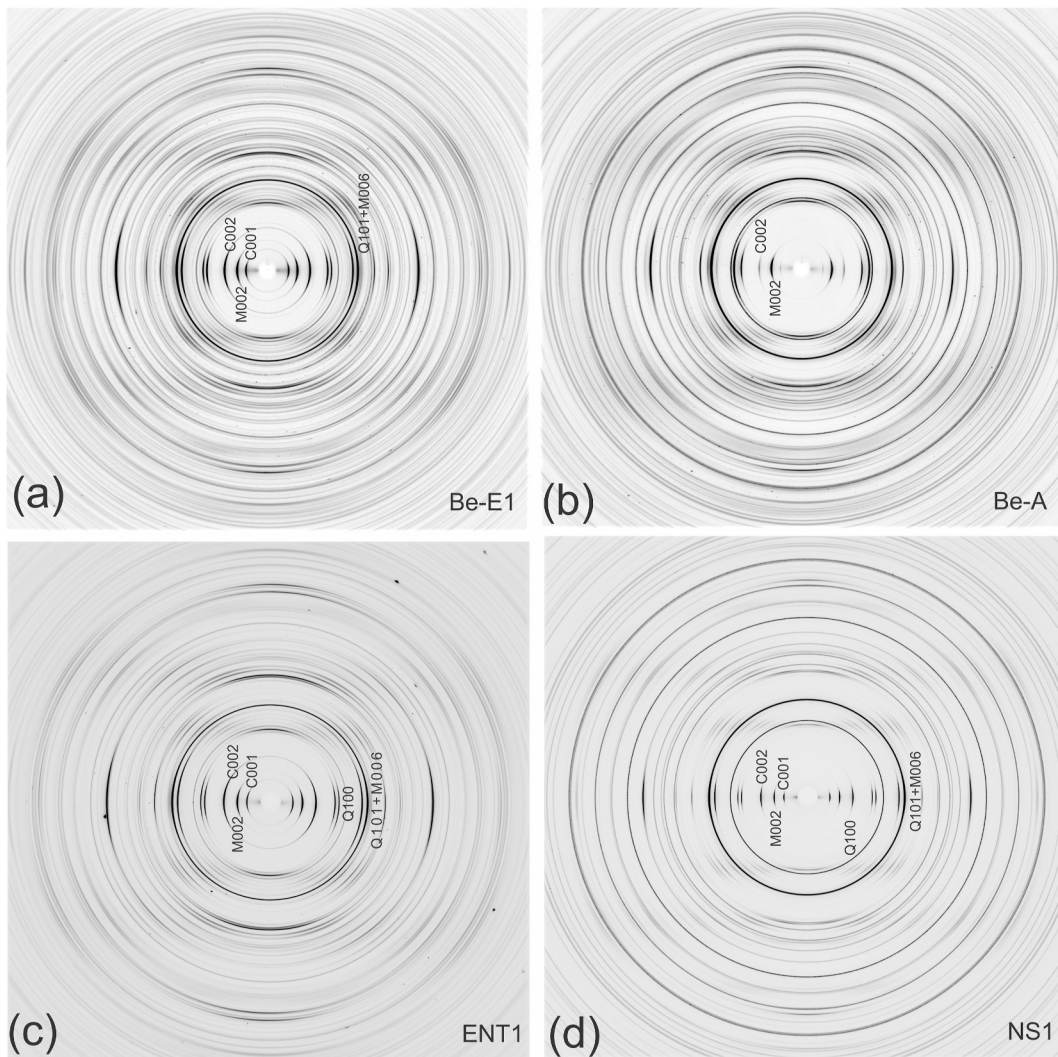


**Fig. 13.** Typical diffraction images for 4 samples. (a) Be-E1 with very strong preferred orientation. (b) Be-A with a broader distribution of phyllosilicates. (c) ENT1 with large fraction of phyllosilicates and a relatively broad distribution. (d) NS1 with strong texture but dominant quartz. These images represent one of 11 from which the texture analysis was done.

volume fractions of components and crystal preferred orientation. Currently the software MAUD (Lutterotti et al., 1997, 2014; Wenk et al., 2014) is the most advanced software for Rietveld texture analysis and applications to some slate samples will be given in section 6.3.

The average over the whole azimuthal range produces a diffraction pattern similar to a powder diffraction pattern on which diffraction peaks and phases can be identified (Fig. SM 1). But for texture analysis we are interested in the azimuthal variation. For slates described in section 6 each image was integrated over  $10^\circ$  azimuthal sectors to obtain a total of 36 “diffraction patterns”. Stacks of all 36 patterns resulting from one image are shown in Fig. 14 with grey shades representing intensities for two slate samples. The strong intensity variations of some reflections (e.g. muscovite Mu 002) with azimuth on the diffraction image (vertical axis in Fig. 14) is representative of preferred orientation, which is also obvious in the diffraction images (Fig. 13). The diffraction patterns are represented as function of  $Q$ .  $Q$  ( $Q = 2\pi/d$ ) is used instead of  $2\theta$  to make it independent of the rather arbitrary wavelength. Notice in Fig. 14 that even for muscovite 200 and chlorite 002 there are small intensities perpendicular to the main maximum, indicating that some of the platy phyllosilicate crystals are orientated perpendicular to the slaty cleavage. (This is consistent with SEM images (Fig. 18 and Fig. SM 2) and will be discussed in section 6.2). ENT1 from Spain (Fig. 14a) shows very sharp diffraction peaks indicating high crystallinity, EPS39A from

the California foothills (Fig. 14b) displays diffuse peaks suggesting a more disordered crystal structure and small grain size. While phyllosilicates are strongly oriented, quartz has no significant intensity variations (e.g. Q 100), suggesting randomly oriented crystal lattices. A comparison of the calculated Rietveld model (Fig. 14 top) with experimental patterns (Fig. 14 bottom) indicates a close similarity, indicative of a good fit, both in intensities as well as position of diffraction peaks.

MAUD calculates three-dimensional statistical crystallographic preferred orientation distribution functions (ODF), relating crystal coordinates of mineral components to sample coordinates. These were exported from MAUD and further processed with Beartex (Wenk et al., 1998) or MTEX (Hielscher and Schaeben, 2008) to obtain, transform and plot pole figures which represent the distribution of lattice plane poles and are represented in spherical projections (section 6). The ODFs are also used to calculate elastic properties (section 8.8).

#### 4.4. SEM electron backscatter diffraction

Local crystal orientations can be measured with the scanning electron microscope (SEM) and this technique has become very popular, both in materials and earth sciences. It was recently applied to the slate variety phyllonite (Wallis et al., 2015). Interaction of the electron beam with the uppermost surface layer of a polished sample produces single

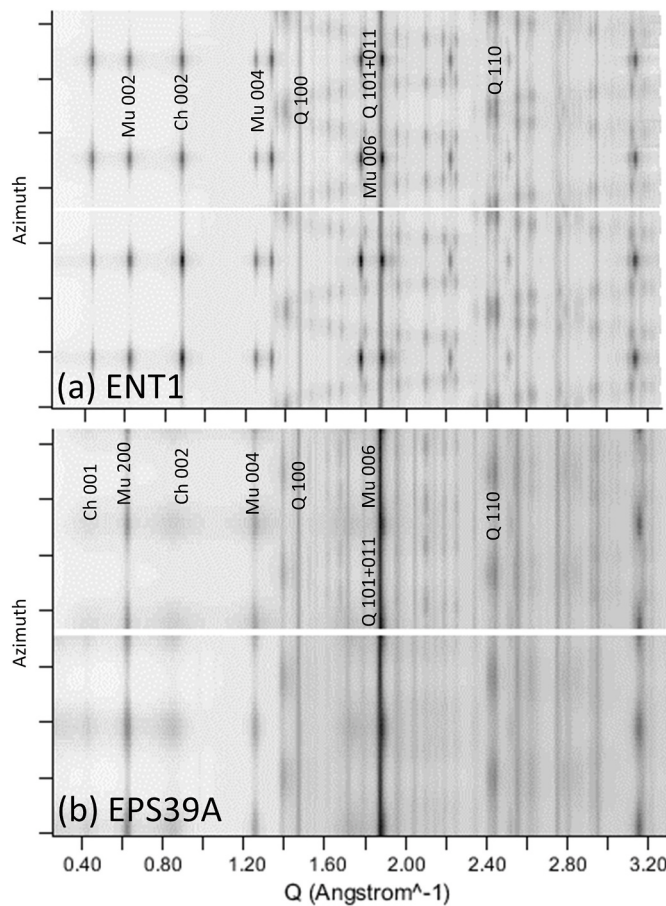


**Figure 14.** “Unrolled” diffraction images (bottom) and Rietveld fit (top) as function of  $2\theta$  integrated over  $10^\circ$  azimuthal sectors. The vertical coordinate is the azimuth on the diffraction image. Intensity differences as function of azimuth are indicative of preferred orientation. Muscovite and chlorite are highly oriented, quartz (with continuous lines) is random. Note the close similarity of observations and model, indicative of a reliable fit. (a) ENT1 with sharp diffraction peaks, (b) EPS39 with highly diffuse peak for chlorite.

crystal electron backscatter diffraction images (EBSD) (Fig. 15a) from which orientations at the sub-micron scale can be determined (e.g. Dingley, 1981; Fig. 15b). By translating the sample or tilting the beam, the surface can be scanned, usually covering a range of  $\sim 1 \text{ mm}^2$ . At each position an EBSD image is recorded, then the digitized image is automatically indexed and the orientation of the crystal is extracted (e.g. Wright and Adams, 1992). On modern systems over 4000 measurements can be performed in a second. EBSD maps contain much more information than bulk X-ray diffraction images, particularly about orientation relationships between grains and misorientations, grain shapes and sizes, domainal fabrics as well as evidence for grain bending. An example of EBSD analysis on slate will be shown in section 7.

EBSD Orientation Imaging Microscopy (OIM) is a modern extension of earlier optical measurements on geological materials (axis distribution analysis, “AVA”, Sander, 1950).

#### 4.5. Magnetic fabric analysis

Another method to identify the preferred orientation in slates is the use of the anisotropy of the low field magnetic susceptibility (AMS) (Borradaile and Henry, 1997; Borradaile and Jackson, 2010). The AMS is related to the orientation distribution of iron-rich rock-forming minerals and their intrinsic magnetic properties. In the case of slates, the magnetic fabric is dominated by paramagnetic chlorite and chloritoid.

Already Wood et al. (1976) found in Cambrian slates of North Wales

(UK) a good agreement between the magnetic fabric and the phyllosilicate preferred orientation obtained by X-ray pole figure goniometry. Typically the minimum principal magnetic susceptibility axis is oriented perpendicular to the cleavage plane. On the other hand, the maximum principal magnetic susceptibility axis is parallel to the fabric lineation (both stretching and intersection lineation). However, there is often a mismatch between the magnetic susceptibility pattern and the phyllosilicate fabric (e.g. Haerick et al., 2013). This may be caused by different magnetic carriers contributing to the magnetic fabric. To interpret such composite magnetic fabrics correctly, it is imperative to understand the contributions of the different minerals to the bulk magnetic fabric (Martin-Hernandez and Hirt, 2003; Biedermann et al., 2014).

#### 5. Early studies of slate preferred orientation

Sander (1950) published a pole figure of (001) muscovite in phyllite from Zillertal (Austria), measured with optical microscopy, and determined a maximum peak density of 11 multiples of random distribution (mrd) (#109) (Fig. 16a). The unit to express pole densities in different directions is to integrate the distribution over the whole sphere and normalize this to 1.0. In a textured material there are directions which are larger than 1 (pole figure maxima) and regions which are lower than 1. In a material with a random orientation distribution, all directions are 1.0. “Random distribution” is also sometimes called “uniform distribution”. This normalization applies both to ODF and to pole figures. However, there can be differences if individual crystals are considered (as with Sander) in the integration, grain volumes (as with X-ray diffraction) or grain surfaces (as with EBSD).

Early investigations of slate fabrics have been reviewed by Oertel (1983). It was Oertel (1970) who first applied pole figure goniometry to study preferred orientation of muscovite in slates and perfected the technique to provide quantitative information represented in (001) pole figures. Emphasis was on slates from Wales and the Lake District in England. (001) pole figures of muscovite in slaty andesite lapilli tuff of Ordovician age documented concentrations up to 8 mrd. Shape of lapilli revealed compaction and subsequent compressive deformation perpendicular to the cleavage plane (Oertel, 1970). The pattern of preferred orientation of muscovite was interpreted based on the March (1930) model that assumes alignment of rigid platelets in a viscous medium (see Section 8.3).

Similar studies on a Cambrian slate from the Penrhyn quarry in N Wales illustrate maxima of (001) poles perpendicular to the slaty cleavage, up to 16 mrd and an ellipsoidal distribution (Fig. 16b) (Oertel and Phakey, 1972). The slaty cleavage on which the pole figure is projected is quite different from the bedding plane indicated by the dashed line. Oertel and Curtis (1972) studied Carboniferous shale from Penistone, England, with (001) maxima for illite and kaolinite up to 9 mrd, attributed to progressive compaction in accordance with shape changes of concretions. The comparison of strain observed in reduction bodies with preferred orientation of muscovite up to 15 mrd was the content of several studies (Tullis and Wood, 1975; Siddans, 1976; Wood et al., 1976; Wood and Oertel, 1980).

Oertel (1974) ingeniously used variations of chlorite preferred orientation in a fold with layers of slate and quartzite from the Inyo Mountains in California to determine strain based on the March concept (March 1930) of rigid particles to unfold the fold. Texture patterns were recorded in 36 points with maxima ranging from 4.7 to 17.6 mrd.

Rumble and Oertel (1979) studied metaclastic rocks from New Hampshire where low grade slates transform to higher grade schists. The strains suggested by shape of deformed pebbles does not relate systematically with alignment of phyllosilicates in the matrix because of extensive recrystallization. Another investigation on the effect of static metamorphism on slates is fabric changes in Michigamme (N Michigan) samples (Ho et al., 2001) where preferred orientation increases with increasing grade from 3.3 mrd to 9.8 mrd. However, with conventional

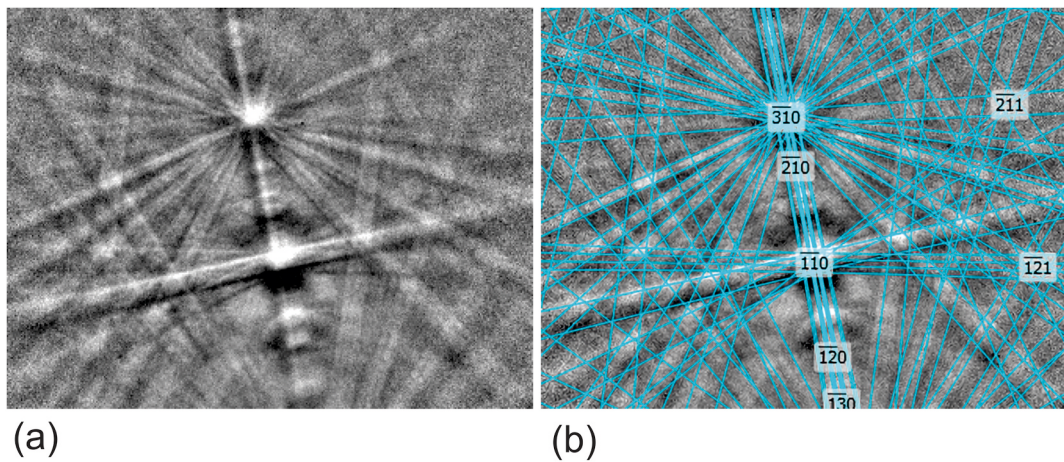


**Fig. 15.** Chlorite EBSD diffraction image of slate BEI from Beiro do Rio (Spain). (a) Raw image, (b) superposed indexed diffractions.

pole figure goniometry muscovite could not be separated from biotite due to peak overlaps and biotite may dominate the high temperature fabric.

Ho et al. (1995) also explored fabric changes in the Lehigh Gap (Pennsylvania) as shale with muscovite and chlorite transforms to slate, and slaty cleavage develops more or less perpendicular to the original bedding plane. In shales the phyllosilicates have an (001) maximum perpendicular to the bedding plane and in slates perpendicular to the cleavage.

Ishii (1988) describes grain growth and re-orientation of phyllosilicates during the development of slaty cleavage in Northern Japan with strong girdle distributions and pole density maxima for illite and chlorite perpendicular to the cleavage ranging from 2 to 8 mrd.

An interesting regional study uses mica preferred orientation in slates to interpret tectonic processes in the Variscan orogeny of Central Europe (Fielitz, 1992). Oblique strike-slip faults develop from pre-existing tectonic boundaries and are influenced by structural trends in the basement. In the Stavelot-Venn basement inlier within the High-Ardenne slate belt in the Eifel region (Germany), Cambro-Ordovician metasediments transformed to slates during tectonic coaxial shortening with qualitative (001) mica pole figures displaying axisymmetric patterns (Fig. 17). Later thrusting resulting in the Monschau shear zone, in which (001) pole figures developed an orthorhombic symmetry, with the short axis of the pole figure pattern parallel to the stretching lineation.

Sintubin (1994) explored cleavage evolution in a Lower Palaeozoic basement inlier within the High-Ardenne slate belt in Belgium,

identifying high-strain zones based on the phyllosilicate preferred orientation. Orthorhombic pole figure patterns superposed on axial symmetrical pole figure patterns is considered indicative of a non-coaxial shear in high-strain zones affecting a pre-existing strong slaty cleavage. The highest pole figure maximum for (001) muscovite is 19.5 mrd and for chlorite is 20 mrd.

A texture analysis of Paleozoic and Mesozoic shales from boreholes in the Campine basin (Belgium) shows that the preferred orientation

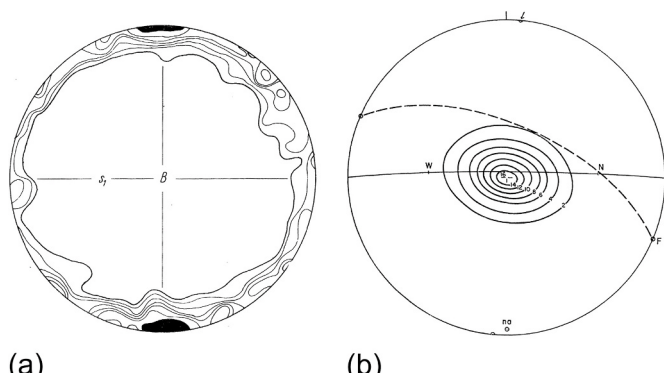


**Fig. 16.** (a) (001) pole figure of muscovite for phyllite from Zillertal (Austria) measured with a universal stage microscope (Sander, 1950, #109). (b) Pole figure of slate from Wales measured with a pole figure goniometer (Oertel and Phakey, 1972). Dashed line is sedimentary bedding plane.

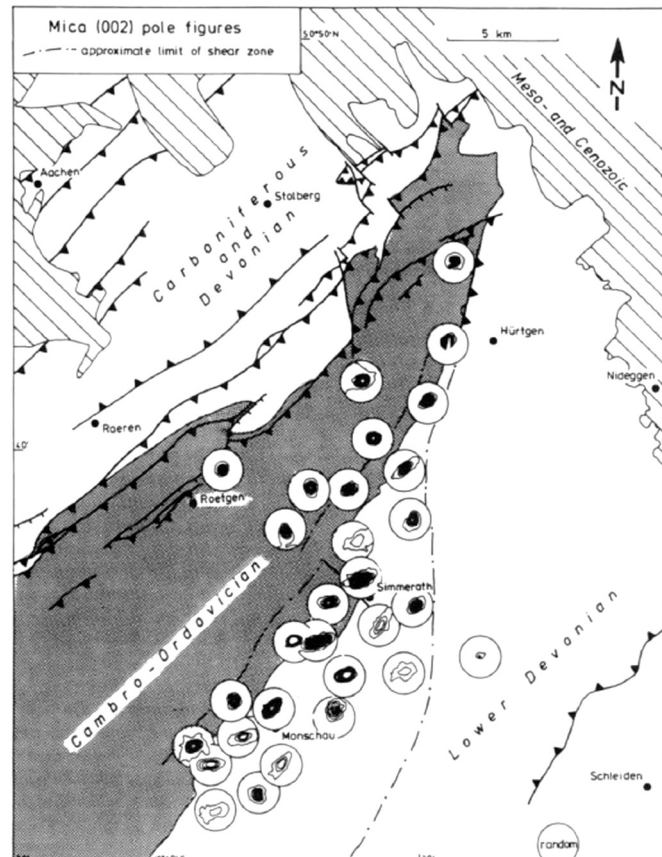


**Fig. 17.** Tectonic map of the Rhenohercian belt of Western Germany with the Stavelot-Venn basement inlier (marked in dark grey). The Cambro-Ordovician unit is covered by the Lower Devonian unit, separated by the Monschau shear zone. Qualitative (001) pole figures of muscovite are indicated, projected on the slaty cleavage (Fielitz, 1992).

**Table 1**

Locations of slate samples used for synchrotron X-ray texture analysis.

(a) European slates	
1	Be-E1
2	Be-E2
3	Be-A
4	Sturtz85
5	Sin2
6	Cz-SLA1
(b) Alps, N Spain, China	
7	Brg 1806e
8	ENT1
9	RZ1
10	Ch1
11	Ch2a
12	Ch2b
(c) Slates from Western US	
13	EPS39A
14	EPS39B
15	DL1
16	NS1
17	NS3
18	DL3

development in shales is independent of the burial depth (Sintubin, 1994), indicating that during the early stages of burial a stable shale fabric develops, which will stay unchanged until a tectonic deformation at low-grade metamorphic conditions leads to the development of a slate fabric.

Sintubin (1996) tracked the cleavage evolution across the frontal fold-and-thrust belt of the Variscan orogen in the Belgian Ardennes by means of phyllosilicate textures, indicating that in low-grade metamorphic deformation conditions rock composition and local strain conditions are controlling the phyllosilicate preferred orientation. The highest pole figure maximum recorded in this survey is 12 mrd for (001) muscovite.

Recently Haerinck et al. (2015) observed a very high degree of anisotropy of magnetic susceptibility (AMS) (1.41) in Paleozoic

muscovite-chloritoid slates from Brittany (France). This was a first application of synchrotron diffraction to slates and documented a (001) pole figure maximum of 21 mrd of chloritoid, explaining the high AMS anisotropy. Muscovite in this sample had a (001) maximum of 39 mrd, two times larger than any previously recorded phyllosilicate texture strength recorded with pole figure goniometry. It lead to a follow-up study of slate from the Ardennes that set a new record with 123 mrd (Wenk et al., 2019), and encouraged us to use the method to survey crystal preferred orientation in a wide range of slates and results will be reported in the next section.

## 6. Survey of slate preferred orientation analyzed with synchrotron X-rays: new records for orientation strengths

### 6.1. Samples

In this section we provide results about slate fabrics investigated with synchrotron X-ray diffraction to explore orientation patterns observed in a variety of geological settings. Samples were collected more or less at random from different parts of the world (Table 1). As mentioned earlier in this context we emphasize preferred orientation and not details about the tectonic or metamorphic histories.

A first set of slates is from Devonian slates in Belgium and Germany: the La Fortelle quarry in the Belgian Ardennes (Be-E1 and Be-E2; e.g. Asselberghs, 1924; Schavemaker et al., 2012), at Ruhrsee, Eifel, Germany (Be-A; e.g. Van Noten et al., 2012), a sample with fossils from the classical Sturtz collection from the lower Devonian Hunsrück formation at Bundenbach, Germany (Sturtz85; e.g. Briggs et al., 1996; Raiswell et al., 2008). One sample is a Silurian slate of the Plougastel Formation of Brittany, France (Sin2; Van Noorden et al., 2007) and one from a quarry of Moravian-Silesian slate deposits at Domasov in the Czech Republic (Cz-SLA1; e.g. Zimak et al., 2002).

One sample is a metasedimentary greenschist slate at the base of the Variscan Grevasalvas granite in the Austroalpine Err/Carungas nappe (Brg 1806e; Cornelius, 1950; Handy et al., 1996). Two samples are from slate quarries in Northern Spain (ENT1, and RZ1, Cárdenes et al., 2014, 2015). Three samples are from China, one collected on floors in Pudong/Shanghai (Ch1) and two from Huangshan City (former Tunxi) in southern Anhui Province (Ch2a, Ch2b). They are probably of Ordovician age and were quarried in Jiangxi Province near Xingzi (e.g.

**Table 2**

Composition (volume fraction %) and texture maxima in parentheses ((001) max-min, in mrd) and for quartz (0001) maximum only. Same order as Table 1. Abbreviations for accessories: Ab albite, Cc calcite, Ap apatite, Ilm ilmenite, Ru rutile, H hematite (volume fractions in parentheses).

	Muscovite	Chlorite	Quartz	Accessories
(a) European slates				
Be-E1	36	(123.3-0.01)	15	(71.2-0.10)
Be-E2	38	(88.9-0.01)	20	(11.4-0.39)
Be-A	40	(4.0-0.05)	15	(4.9-0.03)
Sturtz85	28	(64.3-0.12)	36	(34.6-0.07)
Sin2	47	(36.0-0.02)	18	(39.0-0.03)
Cz-SLA1	35	(7.6-0.3)	22	(7.2-0.2)
(b) Alps, N Spain, China				
Brg1806e	23	(20.0-0.15)	14	(18.0-0.26)
ENT1	33	(31.6-0.07)	42	(19.3-0.07)
RZ1	36	(33.6-0.05)	34	(26.2-0.06)
Ch1	26	(9.6-0.14)	18	(4.0-0.2)
Ch2a	25	(15.0-0.05)	17	(10.0-0.03)
Ch2b	22	(8.2-0.23)	17	(7.4-0.17)
(c) Slates from Western US				
EPS39A	28	(14.0-0.3)	18	(8.4-0.14)
EPS39B	30	(22.3-0.01)	26	(5.12-0.42)
DL1	29	(5.3-0.14)		
NS1	11	(62.6-0.09)	10	(42.3-0.18)
NS3	39	(45.1-0.12)	27	(67.4-0.32)
DL3	44	(19.0-0.05)	10	(8.7-0.02)

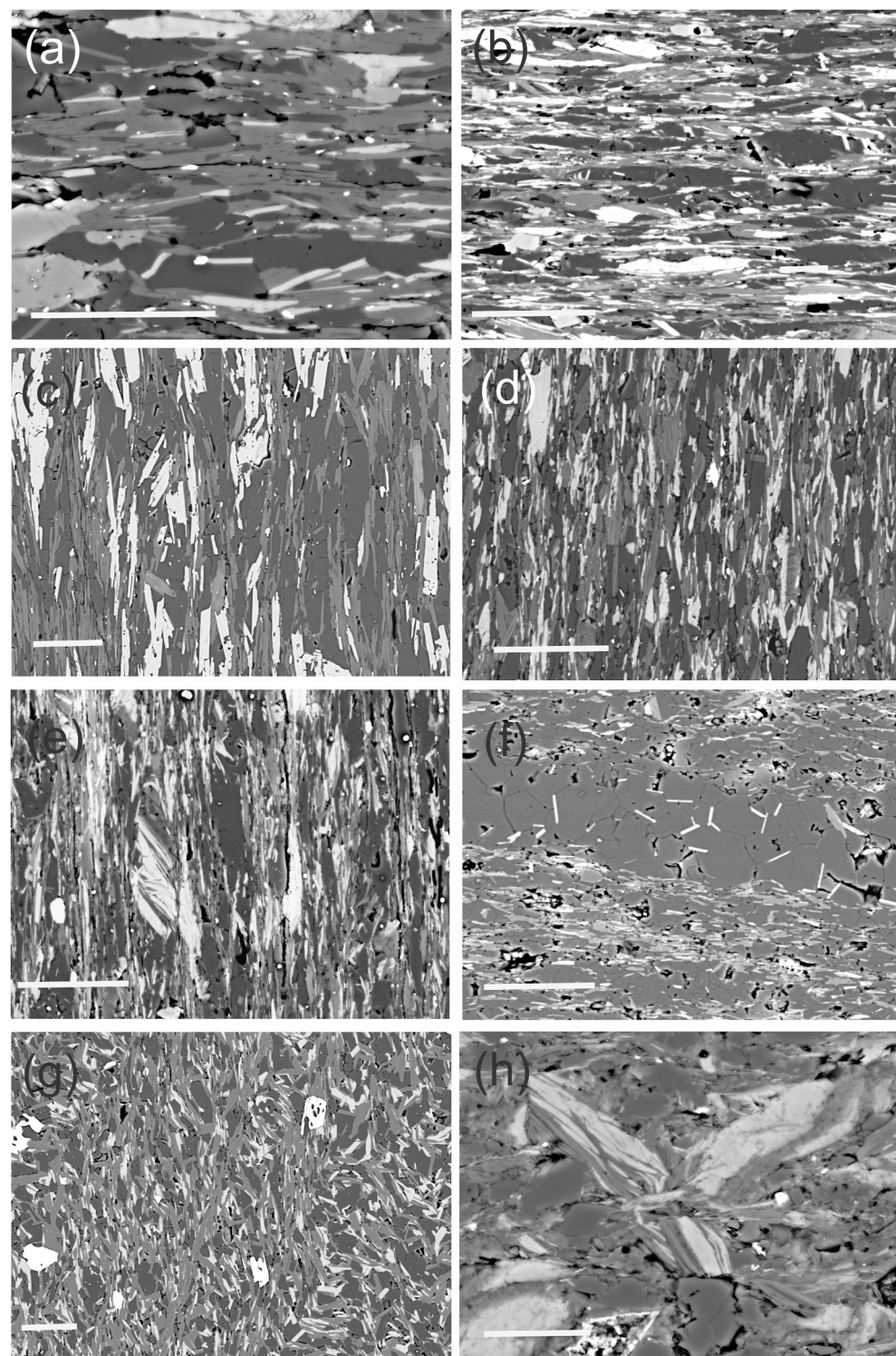


**Fig. 18.** SEM-BE images of selected slate samples. (a) Be-E1 from La Fortelle, Ardennes. Strong alignment of phyllosilicates (grey muscovite, bright chlorite with a kinked crystal above the scale; quartz is dark but also flattened). (b) Slate from Hunsrück, Germany (Sturtz85). (c) Slate Sin2 from Brittany. (d) Slate Rz1 from N Spain with very strong alignment of muscovite and chlorite. (e) Slate Ch1b from China with an assemblage of interlayered muscovite and chlorite. (f) Quartz-rich slate NS1 from Northern California. In a quartz-rich band are euhedral chlorite crystallites. (g) Slate Ch2a from China with crenulations (compare Fig. 5e), (f) Be-A from Ruhrsee, Germany with two cleavages and also here interlayered muscovite and chlorite (compare Fig. 5c). Scale bars 20 µm.

Jinbiao, 2010; Xue, 2002).

The remaining six samples are from Northwestern North-America. Two samples are from the Jurassic Mariposa formation near Angels Camp in the foothills of the Sierra Nevada in California (EPS39A and EPS39B; e.g. Eric et al., 1955; Clark, 1964; Bogen, 1984), one from the Paleozoic Shoo Fly Group near Iron Point, Placer Co. CA (DL1; e.g. Snow and Scherer, 2006), and two slates are from Spanish Creek, N of Quincy CA (NS1 and NS3; e.g. Day et al., 1985, 2004). A Paleozoic slate from the Blade Group is from Black Butte, Pima County, Arizona (DL3).

Most samples display a perfect macroscopic planar cleavage (e.g. Be-E1, Fig. 5a). But in the vicinity of sample Be-E1 are slates that have undergone substantial secondary deformation, resulting in kinking (Fig. 5b). An exceptional sample with two cleavages is from Ruhrsee, Germany, resulting in pencil-shaped morphology (Be-A, Fig. 5c), resembling samples from the Appalachians studied by Engelder and Geiser (1979). The sample from Bundenbach contains well-preserved Aspidosoma tischbeinianum fossils indicating that in this case the cleavage coincides more or less with the sedimentary bedding plane

(Sturtz85, Fig. 5d). Samples from China have a pronounced crenulation lineation (e.g. Ch1, Fig. 5e). Lineations are also well developed in slates from Bundenbach (Fig. 5d), the Czech Republic (Cz-SLA1) and Spain (RZ1).

The main phases in all samples are white mica, chlorite and quartz (Table 2). The volume fractions of major components were determined with the Rietveld refinement as described in section 4.2. The composition of individual phases, including accessories was identified with SEM-EDS. Quartz ranges from 25 to 79 vol%. Muscovite (white mica) is the dominant phyllosilicate (22–47 vol%) and chlorite ranges from 0 to 42%. One sample from China (Ch1) has a significant amount of calcite (7%) and some dolomite. Sample DL3 from Arizona contains 4% of hematite, enough to include it in the texture refinement. There are some accessories as determined by SEM-EDS: many slate samples contain albite (0–18%). Be-E1 and Be-E2 have small amounts of calcite and two generations of chlorite. Sin2, RZ1, EPS39A and DL3 contain rutile, Ch2a and Ch2b have ilmenite, and Cz-SLA1 is rich in sphene. Be-A, Ch1 and Ch2b have apatite and ENT1 has monazite. Mica in EPS39A contains some iron and in Sin2 mica is enriched in Na. Chlorite is often interlayered with mica. Sin2 and Ch1 contain Al–Fe-rich chlorite. EPS39A, EPS39B contain ~11% of illite.

## 6.2. Microstructures

The microstructure is best viewed with backscatter SEM-BSE images (selected images are shown in Fig. 18 and images of all samples are summarized in supplementary material Fig. SM 2). The brightness in SEM-BSE images depends largely on atomic numbers: bright for high atomic numbers such as iron-rich and dark for low atomic numbers such as Si and O (e.g. Reed, 2010). On SEM-BSE images dark is generally quartz, dark grey is white mica (muscovite) and lighter grey is chlorite. Chlorite in Sin1, RZ1 and Ch1 is very bright due to a high Fe-content. Very bright colors are ore minerals such as pyrite. Black colors are pores, some introduced during sample preparation.

In many samples phyllosilicates have a fairly euhedral geometry and are not bent (Fig. 18a, c, d, f; Fig. SM 2-a2, a5, b7, b8, b9, b12, c16, c17). The slates from the Sierra Nevada foothills in California (EPS39A, EPS39B and DL1) shows a crenulation cleavage, indicative of secondary deformation, with some alteration to illite-smectite (Fig. SM 2-c13, c14,

**Table 3**

Width of (001) texture peak at half maximum ( $^{\circ}$ ), ratio in parentheses, average grain aspect ratio (large/small) from microstructures (Fig. 5).

Sample	Muscovite		Chlorite		Quartz
	Width	Aspect	Width	Aspect	
(a) European slates					
Be-E1	4/4 (1)	14	9/9 (1)	13	7
Be-E2	6/8 (1.3)	15	22/27 (1.2)	18	5
Be-A	30/130 (4.3)	10	35/89 (2.5)	10	1.5
Sturtz85	14/14 (1)	18	18/23 (1.3)	21	9
Sin2	16/21 (1.3)	25	18/21 (1.2)	20	9
Cz-SLA1	18/27 (1.5)	11	21/36 (1.7)	5	3
(b) Alps, N Spain, China					
Brg1806e	16/25 (1.6)	12	16/29 (1.8)	7	6
ENT1	18/21 (1.2)	25	22/25 (1.1)	16	8
RZ1	15/20 (1.3)	21	17/21 (1.2)	22	6
Ch1	26/49 (1.9)	15	39/77 (2.0)	4.5	5
Ch2a	15/39 (2.6)	25	14/50 (2.6)	12	4
Ch2b	20/60 (3.0)	10	37/61 (1.6)	20	5.5
(c) Slates from Western US					
EPS39A	15/26 (1.7)	6	18/39 (2.2)	6	2
EPS39B	19/26 (1.4)	7	22/36 (1.6)	25	5
DL1	35/42 (1.4)	14	No Chl	4	
NS1	6/16 (2.7)	6	14/14 (1)	9	2.5
NS3	6/10 (1.7)	8	12/12 (1)	11	4
DL3	24/24 (1)	7.5	22/26 (1.2)	Little Chl	4

c15). The pencil cleavage (Fig. 5c), caused by the superposition of two cleavages (Be-A) is exceptional, with different phyllosilicate orientations (Fig. 18h, Fig. SM 2-a3).

Occasionally there is interlayered growth of muscovite and chlorite (e.g. Fig. 18b,c,e, h and Fig. SM 2-a1 Be-A, a4 Sturtz85, b9 RZ1, b10 Ch1, c14 EPS39B and b11 Ch2a). In sample Ch2a, with a macroscopic intersection lineation, there is some evidence for kinkbands with bending, creating a crenulation cleavage (Fig. 18g).

Quartz has in most samples a flattened shape (Fig. 18) except for the quartz band in Fig. 18f with a polyhedral microstructure. In most samples quartz is surrounded by phyllosilicates. From SEM images an average aspect ratio was derived which ranges for quartz from 9:1 to 2:1 (Table 3), compared with 20:1 to 6:1 for phyllosilicates. Accessories such as calcite, monazite, rutile and titanite are fairly equiaxed.

## 6.3. Preferred orientation of phyllosilicates

In this section we discuss crystallographic preferred orientation (CPO). (001) and (010) pole figures in equal area projection on the cleavage plane for white mica and chlorite are shown in Fig. 19. This orientation is optimal for phyllosilicate pole figures because the distribution of the most important element – the (001) distribution – is least distorted. Additional information is summarized in Tables 2 and 3. Note that for texture analysis of monoclinic crystals such as muscovite and monoclinic chlorite the “first-setting” needs to be applied in MAUD, i.e. (100) is the cleavage plane, instead of a more familiar “second-setting” with (001) as the cleavage plane (Matthies and Wenk, 2009). But for labels of lattice planes  $hkl$  in text, tables and figures we use the more conventional second setting. For pole figures colors are used to represent pole densities and the same pole density scales are applied to all samples which makes it easy to assess the wide range of patterns. Logarithmic scales are used for phyllosilicates (Fig. 19) and linear scales for quartz (Fig. 20). Samples with red maxima and white minima have strongly aligned phyllosilicates.

For muscovite the (001) pole figure maxima vary from 4 mrd (Be-A) to 123 mrd (Be-E1) and for chlorite from 4 mrd (Ch1) to 71 mrd (Be-E1). Plotting the (001) maxima of muscovite versus chlorite, one can observe a rough correlation (Fig. SM 3). This is also confirmed by the microstructures (Fig. 18).

In samples with high CPO for muscovite and chlorite (Be-E1, Be-E2, Sturtz85, Sin2, Brg 1806e, ENT1, DL1, NS1, NS3, DL3), the orientation distribution of the (001) poles has more or less axial symmetry. Also the (010) pole figures show an axial symmetry, inferring that there is no a-axis CPO present in these samples and there is a rotational freedom about the (001) pole of phyllosilicate platelets in the cleavage plane (Fig. 19).

In other samples (001) pole figures show an orthorhombic symmetry with the (001) maximum spread out, in some cases even defining a girdle (e.g. Be-A, Ch2a and Ch2b in Fig. 19). For most samples muscovite and chlorite pole figures have (001) maxima at the same position. An exception is Ch1 where the muscovite maximum is perpendicular to the cleavage plane but the chlorite maximum is significantly inclined (Fig. 19). However, the chlorite texture is much weaker than muscovite. This is the only sample that shows a significant deviation from an orthorhombic symmetry pattern of phyllosilicate pole figures.

The (001) texture maximum can be further quantified by determining the angular width at half-maximum of the texture peak (Table 3). This is a single number for axially symmetric textures and two numbers for girdle textures with an ellipsoidal distortion. For axially symmetric ones, the width ranges from 4° to 20° (Fig. SM 3). For the orthorhombic distributions the short width (at half-maximum) ranges from 14° to 43°. Muscovite and chlorite show very similar distributions (Fig. SM 4).

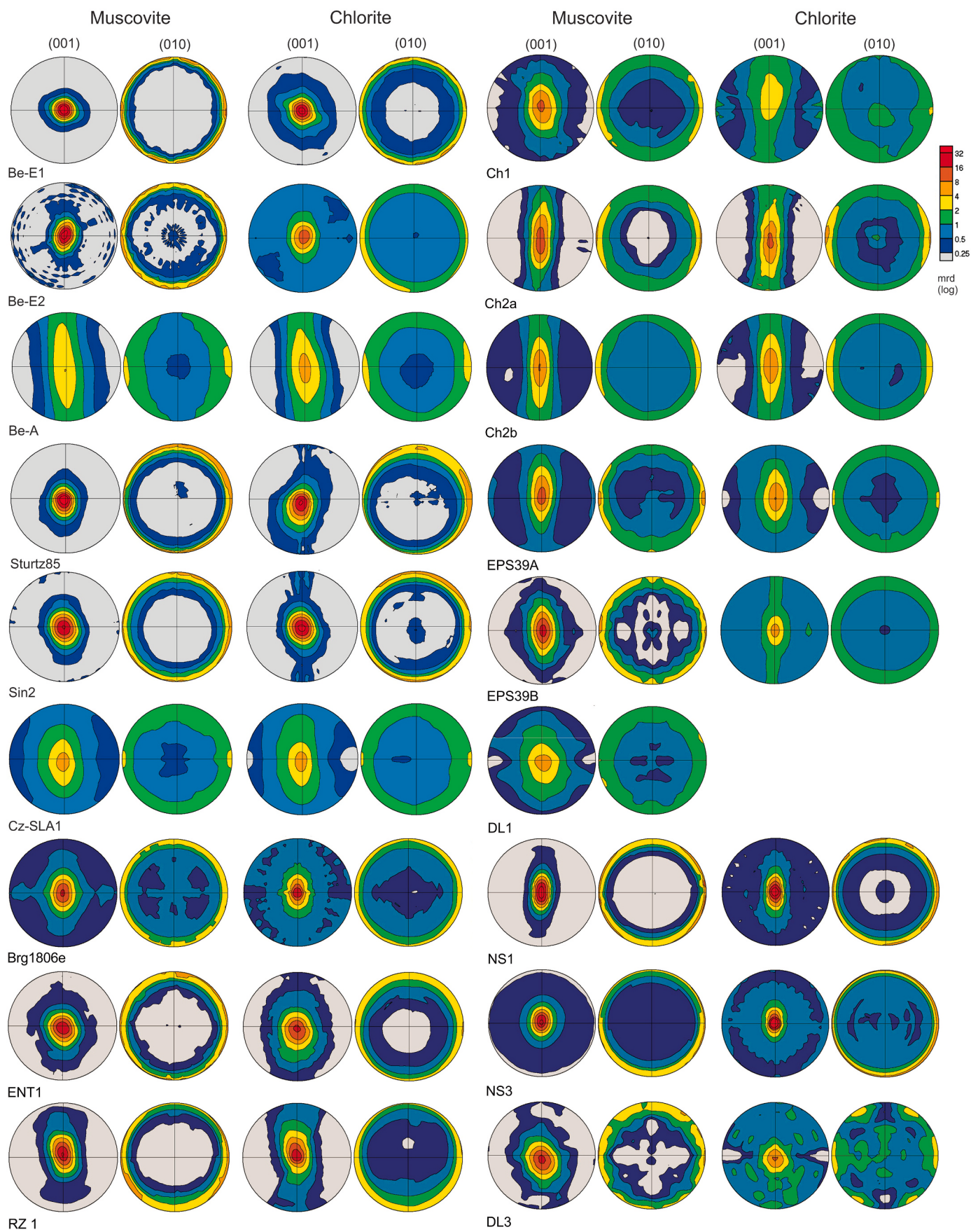


**Fig. 19.** Preferred orientation of white mica and chlorite. Samples in same order as in Table 1. (001) and (010) pole figures projected on cleavage plane in equal area projection. Contours in multiples of random distribution (mrd). Logarithmic intensity scale.

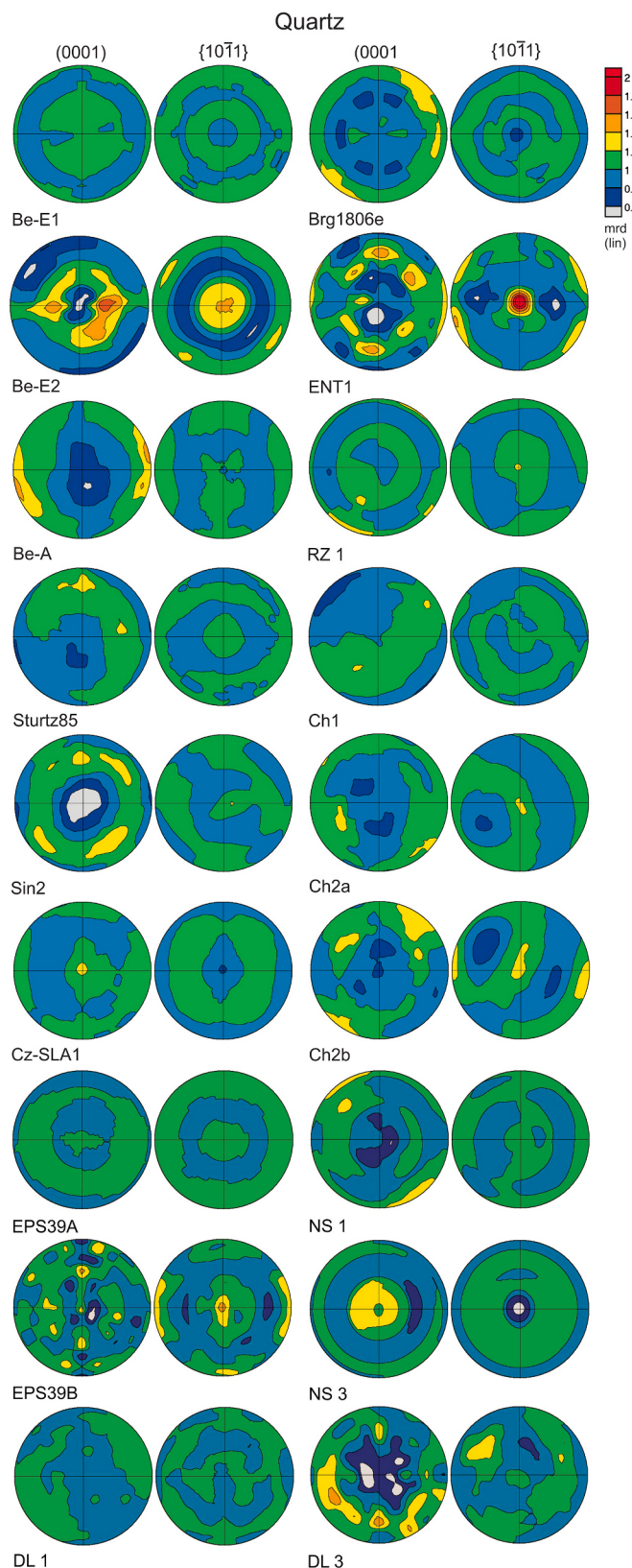


**Fig. 20.** Preferred orientation of quartz. Samples in same order as in Table 1. (0001) and (10–11) pole figures projected on cleavage plane in equal area projection. Contours in multiples of random distribution (mrd). Linear intensity scale.

#### 6.4. Preferred orientation of quartz and accessories

Perhaps most surprising has been the effective absence of significant preferred orientation for quartz (Fig. 20), in spite of the highly flattened shape (Fig. 18, Table 3). Variations between 0.6 (light blue) and 1.4 mrd (yellow) are most likely artifacts of the Rietveld analysis with extremely oriented phyllosilicates and diffraction peaks overlapping with quartz. A relatively high CPO was observed in Be-A (with the weakest phyllosilicate texture), with c-axes preferentially aligned in the lineation direction (1.5 mrd, Fig. 20). The maxima of positive rhombs ( $10\bar{1}1$ ) perpendicular to the cleavage plane could be conceivably be attributed to mechanical Dauphiné twinning (e.g. Be-E2 with a 1.5 mrd maximum and ENT1 with a maximum of 2.3 mrd, Fig. 20) but also this is not conclusive since diffraction from positive and negative rhombs overlap in the same diffraction peak and may be difficult to separate, given the superposition from strongly oriented phyllosilicates.

Only one sample, Ch1, has a significant amount of calcite (7%) and here calcite does display preferred orientation, with a (0001) maximum perpendicular to the cleavage (1.8 mrd, Fig. SM 5a). In DL3, with 6% hematite, the texture displays a fairly strong (0001) maximum perpendicular to the foliation (15 mrd, Fig. SM 5b).

#### 7. Investigation of CPO with EBSD

Electron backscatter diffraction (EBSD), as introduced in section 4.4 is a technique that allows collecting the full crystal orientation of different mineral phases in areas as large as tens of  $\text{mm}^2$  with a scanning electron microscope (SEM). The main strength of EBSD is the ability to characterize materials by directly linking microstructure and the full crystallographic texture. For example, by characterizing and locating grain boundary types, including epitaxial relationships and establishing links between crystallographic orientation and the grain size, shape and/or intracrystalline plastic deformation. State-of-the-art EBSD systems have spatial resolutions down to tens of nanometers, and angular resolution within the  $0.1\text{--}0.5^\circ$  ( $<0.01^\circ$  using HR-EBSD) (e.g. Wilkinson et al. 2006; Wallis et al., 2016). Many SEM-EBSD systems also allow the acquisition of EDS (Energy-dispersive X-ray spectroscopy) maps simultaneously, enabling complementary compositional and microstructural data to be obtained. The main limitation of the EBSD method is that it operates on surfaces and therefore inherits all the limitations inherent to section-dependent techniques (e.g. apparent grain sizes).

In the past phyllosilicates and clays suffered from severe misindexing problems limiting the application of EBSD in slates (Valcke et al., 2006). Nowadays, the problem of misindexation in mica-rich rocks mainly lies in the quality of sample preparation. Recent studies proved that with careful preparation EBSD is a suitable technique for determining phyllonite textures and microstructures with similar composition and grain size as slates (e.g. Wallis et al., 2015).

Here we choose a sample (BEI) of a green slate from a quarry in Beira do Rio, NW Spain, to demonstrate the applicability of EBSD. The EBSD analysis was performed at Montpellier University, using a Camscan Crystal Probe X500FE, with an accelerating voltage of 20 kV, and a step size (pixel length) of 0.8  $\mu\text{m}$ . Resulting data were processed with MTEX v.5.2 (Hielscher and Schaeben, 2008; Klein et al., 2010). An SEM-BE image is shown in Fig. 21a. Main components are flattened quartz (dark grey), fairly equiaxed albite (darker grey), muscovite (brighter grey) and chlorite (bright grey), similar to microstructures in Fig. 18. The area displayed in Fig. 21b was scanned at 0.8  $\mu\text{m}$  steps and a typical diffraction image for chlorite has been shown in Fig. 15. Based on diffraction images and EDS data 8 phases could be identified, dominantly quartz (26%, 216036 spots), muscovite (24%, 198501 spots), albite (21%, 175386 spots), and chlorite (14%, 116312 spots). The coverage of indexed diffraction patterns is 87% (109888 spots could not be indexed). We can immediately see the distribution of quartz (blue) with flattened grains (aspect ratio  $\sim 1:3$ ) and also the distribution of

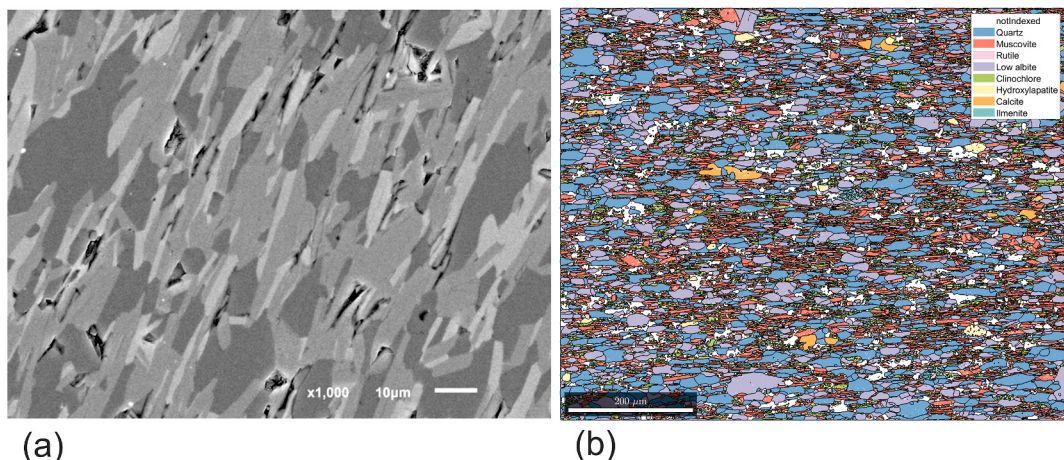


**Fig. 21.** (a) SEM-BE image of slate BEI from Beiro do Rio (Spain). Dark grey is albite, lighter grey quartz, light is muscovite and very bright chlorite. Scale bar 10  $\mu\text{m}$ . (b) EBSD map with identified phases indicated by color. Note flattened quartz grains (blue), muscovite (orange) in clusters and chlorite fine-grained (green). Cleavage is horizontal. Scale bar is 200  $\mu\text{m}$ .

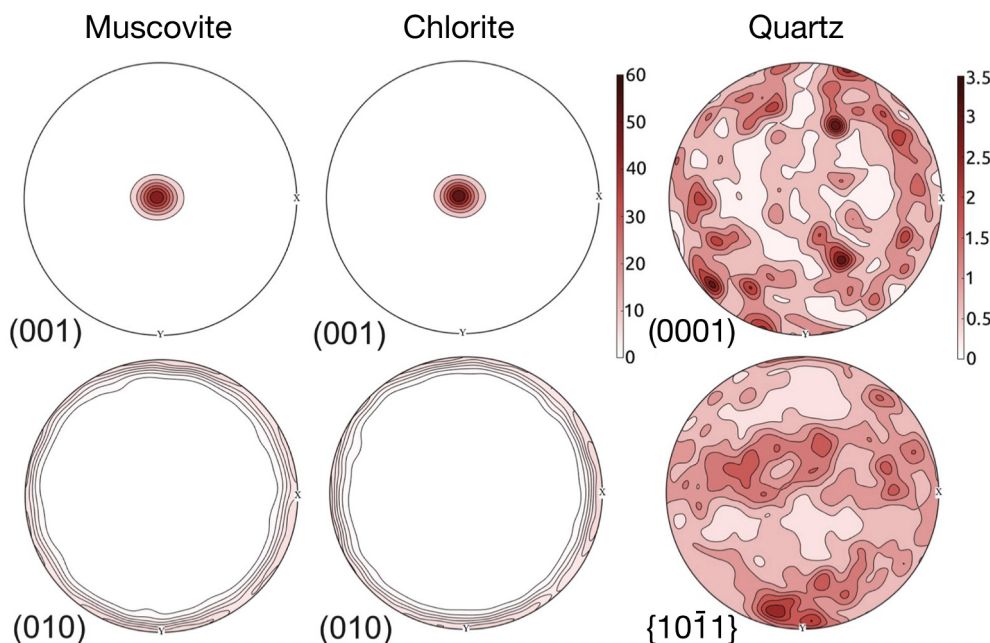


**Fig. 22.** EBSD pole figures of sample BEI from Beiro de Rio (Spain). (001) and (010) pole figures of muscovite and chlorite, (0001) and (10 $\bar{1}$ 1) pole figures of quartz. Equal area projection on slate cleavage. Linear contour scales.

muscovite (orange) clustered in domains.

Pole figures for (001) and (010) of muscovite, and (0001) and (10 $\bar{1}$ 1) of quartz are shown in Fig. 22. Muscovite has an (001) maximum of 51 mrd, chlorite of 58 mrd, averaging all measured orientations over all grains. Pole figures for quartz display basically a random orientation distribution, similar to X-ray diffraction measurements. There is no apparent maximum for 10 $\bar{1}$ 1 perpendicular to the cleavage.

## 8. Discussion

### 8.1. Extreme preferred orientation of phyllosilicates compared with earlier studies

Applying new quantitative methods of texture analysis based on high energy synchrotron X-ray diffraction developed for shales (e.g. Wenk et al., 2014) and SEM-EBSD for phyllonites (Wallis et al., 2015) revealed extreme preferred orientation of mica in slates, much stronger than

reported in previous investigations using a pole figure goniometer. For some samples it exceeds any reported preferred orientation in rocks and is even higher than preferred orientation in recrystallized metals that was the previous record (e.g. Hutchinson and Nes, 1992). This is extraordinary, since slates are fine-grained polyphase materials.

With all the interest in slates, slaty cleavage and slate properties it is surprising that there is not more quantitative information about crystal preferred orientation. Early studies with X-ray pole figure goniometers were described in section 5. In investigations of slates from Wales (001) maxima of muscovite range from 2 to 16 mrd (Oertel, 1970; Oertel and Phakey, 1972; Tullis and Wood, 1975; Siddans, 1976; Wood and Oertel, 1980), in California slates 5 to 18 mrd (Oertel, 1974), in Michigamme slates from 3 to 10 mrd (Ho et al., 1996) and in Belgian slates from 3 to 20 mrd (Sintubin, 1994, 1996). With synchrotron diffraction and Rietveld image analysis we find a range from 4 to 123 mrd, with 8 samples exceeding 30 mrd. The main reason probably is that previous studies relied on pole figure goniometry which has limitations for fine-grained

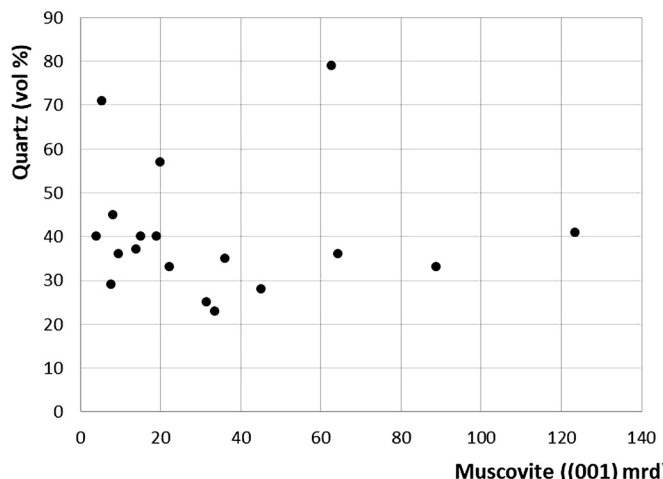


Fig. 23. Plot of quartz content (volume %) as function of (001) maximum of muscovite in slates (from Table 2).

polyphase materials with very strong textures, particularly overlapping diffraction peaks, limitations in intensity corrections and difficulties in estimating the background.

The EBSD analysis of a sample from N Spain (Fig. 22) is remarkably similar to synchrotron X-ray analysis of Spanish slates (ENT1 and RZ1), with maxima ranging from 30 to 40 mrd (Fig. 19).

Fig. 23 is a plot of quartz volume fraction versus (001) muscovite texture strength. It demonstrates that there is no direct relationship. Samples with a very high phyllosilicate content can have strong textures (e.g. Sin2 with 65% phyllosilicates and an (001) maximum of 36 mrd for muscovite) but low phyllosilicate content can also produce strong textures (e.g. NS1 with only 21% phyllosilicates and an (001) maximum of 63 mrd). Other factors that have not been considered in this study, such as the tectonic history and metamorphic grade that may be related to texture strength and pole distributions. Samples with strong lineations and crenulations display girdle-like textures.

The strength of muscovite preferred orientation correlates with the texture peak width (at half maximum) that ranges from 4 to 35° (Table 3, Fig. SM 3). Muscovite and chlorite texture maxima are correlated (Table 2, Fig. SM 4), though for weak preferred orientation chlorite may be stronger than muscovite but this should be explored further with well-defined samples from similar localities.

#### 8.2. Absence of significant CPO of quartz

Quite surprising has been the effective absence of significant crystal preferred orientation (CPO) for quartz (Fig. 20, 22), in spite of a highly flattened shape (SPO) (Figs. 18 and 21, Table 3). Concentrations of <1.5 mrd are most likely artifacts of the Rietveld analysis with extremely oriented phyllosilicates and diffraction peaks overlapping with quartz. There is no systematic orientation of positive rhombs in the foliation plane that could be attributed to mechanical Dauphiné twinning (e.g. Minor et al. 2018), except perhaps for Be-E2 and ENT1. In the literature of slates there has been not much discussion about quartz CPO in slates (Attewell and Taylor, 1969, is an exception).

#### 8.3. Suggestion of mechanisms leading to such extraordinary fabrics: March-Jeffery model

There are a few experimental studies to investigate fabric development in slates and slate analogs (e.g. Means and Paterson, 1966; Paterson and Weiss, 1966; Tullis, 1976). But experiments are difficult because they cannot reproduce the slow processes occurring at low temperature such as growth and dissolution.

Some models have been developed to describe texture development

by grain-shape-induced rotation processes. Jeffery (1923) describes the dynamic orientation behavior of rigid, non-equiaxed, particles in a deforming viscous medium. March (1932) uses this concept to infer strain from the orientation pattern of planar, passive markers, deforming homogeneously with the viscous medium. Tullis (1976) showed that the Jeffery model becomes identical to the March model when the rigid particles attain an infinite oblate morphology.

The March model relates the phyllosilicate texture (pole density) with the finite strain ellipsoid, following the equation:

$$\epsilon_i = \rho_i^{-1/3} - 1$$

with the strain  $\epsilon$  ( $= \Delta l/l$ ), the pole density  $\rho$  (in mrd), and the three principal directions  $i$  (1, 2, 3).

Applying this simple relationship is subject to a number of constraints: (1) the orientation distribution has to have at least an orthorhombic symmetry; (2) the initial orientation distribution is assumed to be random; (3) the marker grains are passive geometrical markers; mechanical properties of the marker grains are ignored as well as their position in the material; grain interaction is excluded; (4) deformation is homogeneous; (5) the orientation distribution reflects the total finite strain; (6) there is no volume change during deformation.

It is clear that these constraints do not apply to real materials. Oertel (1983) extensively discusses the significance of the different assumptions for the application of the March model to geological materials. In spite of the above-mentioned constraints, the application of the March model for strain estimates in geological materials has produced impressive results in cases where independent strain markers were available, such as lapilli (Oertel, 1970), reduction spots (Tullis and Wood, 1975) or crinoids (Weber, 1981).

Considering the individual phyllosilicate grains in the slate fabric, it is obvious that their orientation behavior is determined by inter- and intracrystalline processes, and is thus far from Marchian. But, on the average, every phyllosilicate grains seems to show a Marchian behavior, behaving like passive markers rotating in a homogeneously deforming medium. In this respect the Marchian behavior complies with the original definition of a cleavage, being a planar fabric produced by the statistical preferred alignment of platy fabric elements (Ramsay and Huber, 1983).

The Jeffery-March approach relies on a viscous medium and rigid particles which may be applicable to shales where platy phyllosilicates settle in water at surface conditions (e.g. Wenk et al., 2017) as well as deep oceanic environments (e.g. Hornby, 1998; Vasin et al., 2013). This alignment is increased during compaction as observed in natural environments (e.g. Lonardelli et al., 2007; Sintubin, 1993) as well as experiments (e.g. Clark, 1970; Means and Paterson, 1966; Voltolini et al., 2009).

#### 8.4. Recrystallization and dissolution under stress

The microstructures in slates with relatively euhedral muscovite crystals, occasionally interlayered with chlorite in a matrix of much stronger quartz, are more compatible with a mechanism that emphasizes recrystallization and dissolution under stress. Growth under stress can be controlled by thermodynamic considerations (e.g. Kamb, 1959; Paterson, 1973; Ortoleva et al., 1982; Lee et al., 1986; Shimizu, 1992) to predict alignment during recrystallization. Muscovite is elastically highly anisotropic with a stiffness parallel to the (001) plates more than three times higher than perpendicular to it (e.g. Vaughan and Guggenheim, 1986). Quartz is also anisotropic, not quite by a factor two, but there are three stiff  $\{10\bar{1}1\}$  directions and three soft  $\{10\bar{1}1\}$  directions, more or less at right angles (e.g. Heyliger et al., 2002). Thus if phyllosilicates recrystallize in shales, platelets would preferentially align perpendicular to the principal compressive component. Microstructures indicate that muscovite and chlorite grow by replacing surrounding quartz, with no indications of significant rotations during progressive

growth.

Dissolution under stress in sedimentary and low-grade metamorphic rocks has been described by many authors (e.g. Weyl, 1959; von Plessmann, 1964, 1966; Durney, 1972; Rutter, 1976; De Boer, 1977; Sprunt and Nur, 1977) and was applied to quartz (e.g. Powell, 1972; Morris, 1981; Wright and Platt, 1982). This dissolution is most likely responsible for the flattened quartz grain shape (e.g. Knipe and White, 1977; White and Knipe, 1978; Knipe, 1979, 1980) with dissolution and reprecipitation.

Strain has been explored based on the elliptical shape of quartz in slaty rocks from the Ardennes (Mukhopadhyay, 1973), estimating a shortening of 30–80%. Flat shapes of quartz caused by dissolution have also been described in siliceous sediments from Svalbard, Norway (Morris, 1981). However, if these grain shapes develop by dissolution grain shapes may not be an adequate strain estimate, like spherical radiolaria deforming into ellipsoids (e.g. Galvez and Orozco, 1979; Tourniemi et al., 1988).

#### 8.5. Significance of organic components

Sample DL1, a slate from the extensive Paleozoic Shoo Fly Formation in Northern California is a special case. The selected sample has a high quartz and mica content and displays only a moderate muscovite texture (5 mrd, Fig. 19c). This sample is adjacent to layers with high carbon content. Both have excellent cleavage but the latter display no significant preferred orientation and organic carbon may also reduce preferred orientation in DL1. “Organic” slates/shales, or argillites have been described in coal deposits, but very little is known about the transition of siliceous slates into carbon-rich rocks and corresponding microstructures and textures (e.g. Robinson, 1971; Large et al., 1994; Suarez et al., 2012; Taylor et al., 1991).

#### 8.6. Multiple stages of deformation

The original slate orientation pattern may have been modified by different stages of tectonic events as secondary development of a pencil cleavage fabric at Ruhrsee. Phyllosilicates are interlayered in some larger muscovite-chlorite aggregations (Be-A, Cz-SLA1 and EPS39A, Fig. 19). Some slates do contain shear zones with macroscopic kinks (e.g. Ch1 and Ch2a) and do represent crenulation cleavage (e.g. Cosgrove, 1976; Gray and Durney, 1979; Weber, 1981). Bending of phyllosilicates has been documented by TEM (e.g. White and Knipe, 1978; Knipe, 1981; van der Pluijm et al., 1998) as well as SEM (Walsh, 2007).

The deviation of (001) pole figures of phyllosilicates from axial symmetry was quantified with the ratio large/narrow width, given in Table 3. The narrowest width of the 001 peak for muscovite is plotted as function of the total texture strength in Figure SM 4. The majority of the samples show a nearly axial symmetrical orientation distribution (ratio

between 1 and 2). Four samples show a very high ratio, ranging from 2.6 to 4.3 (Be-A, Ch2a, Ch2b, NS1).

The (010) pole figures show a maximum at 90° to the (001) girdle, representing a zone axis (Housen et al., 1993). This zone axis is not generated by an alignment of (010) but by the girdle distribution of (001) poles (Sintubin, 1998). Macroscopically, the zone axis is expressed as an intersection lineation or as the long axis of a pencil cleavage (Fig. 5c). This pole figure pattern is a typical of transformation textures, representing a polymodal orientation distribution of the phyllosilicates (Sintubin, 1993; 1996).

#### 8.7. Comparison of CPO in slates with shales and gneiss

There is general agreement that most slates originate from clay-rich sedimentary rocks. Shale preferred orientation has been of much interest because of the significance for hydrocarbon exploration. Phyllosilicate textures in shales generally are axially symmetric and form largely during sedimentation and subsequent compaction. An example is Kimmeridge shale from the North Sea (Fig. 24a). Typical (001) maxima of illite-muscovite in shale range from 2 to 6 mrd (e.g. Sintubin, 1993; Lonardelli et al., 2007; Wenk et al., 2010; Kanitpanyacharoen et al., 2012; Vasin et al., 2013, Wenk and Vasin, 2017). But sedimentary microstructures observed in compacted shales are generally not preserved in slates. Particularly there is no waviness of phyllosilicates that is common in shales (e.g. Vasin et al., 2013, their Fig. 1). In some slates the original bedding plane is preserved with markers such as fossils (Fig. 5d) or compositional layering oblique to the cleavage (Fig. 2). Clearly the CPO in shales is much weaker than in slates.

Rocks of similar composition, some of which may have transformed from slates at higher metamorphic grade, are schists and gneiss. There is a wide variety of schists and gneiss, in composition, microstructures and metamorphic grade. They are much coarser than slates and, to sample large representative volumes, textures are often investigated with neutron diffraction. Some gneiss is transformed from granite and has a high content of feldspars. Gneiss has a relatively low mica content. Quartz generally does not show significant SPO but has a significant texture attributed to plastic deformation.

Ullmeyer et al. (2006) describe gneiss samples from the Central Alps with a mica (001) CPO up to 4.3 mrd and quartz (001) 1.7 mrd. In highly foliated Tambo gneiss, also from the Alps (001) of muscovite is 3.6 mrd (Fig. 24c), of quartz 1.6 mrd and of plagioclase 2.5 mrd (Vasin et al., 2017). In gneiss from the Outokumpu drillhole in Finland biotite CPO reaches 23 mrd and quartz 2 mrd. For mylonitic gneiss from Montalto (S-Italy) muscovite ranges from 2 to 4 mrd and quartz 2–3 mrd (Fazio et al., 2017). In this study results obtained with different methods, optical, EBSD and time-of-flight neutron diffraction vary considerably. In recrystallized mylonitic gneiss from Palm Canyon (S California) biotite is up to 2.5 mrd, while quartz exceeds 8 mrd (Pehl and Wenk, 2005).

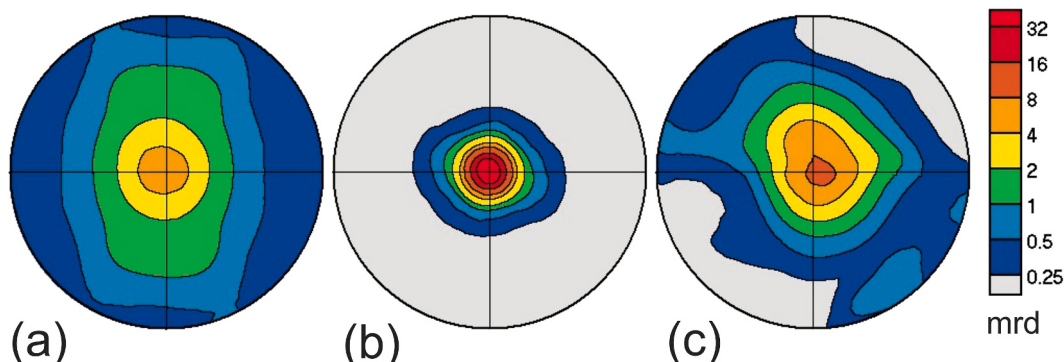


**Fig. 24.** Comparison of muscovite (001) pole figures of (a) Kimmeridge shale (Vasin et al., 2013), (b) Ardennes slate (Wenk et al., 2019), (c) Tambo gneiss (Vasin et al., 2017). Equal area projection on foliation plane. Logarithmic contours.

In all these gneiss samples phyllosilicate textures are relatively weak compared with slates (Fig. 24b). They deform largely by dislocation glide and associated recrystallization.

#### 8.8. Seismic anisotropy based on CPO

The strong crystal alignment in many slates is expressed in anisotropy for seismic wave propagation. Already early experiments (e.g. Christensen, 1965) describe P-wave velocities in slate from Vermont, with velocities perpendicular to the cleavage over 20% slower than in the foliation plane. This was later confirmed for other samples (e.g. Godfrey et al., 2000). Fig. 25 shows velocity patterns obtained by calculating anisotropic elastic properties based on mineral composition and preferred orientation distributions for samples from the Ardennes (BE-E1) and from China (Be-2a). Averaging was done with a geometric mean over all orientations and phases but not taking grain shapes or porosity into account (Vasin et al., 2013). Both samples have over 50% quartz with a random orientation distribution and yet the seismic anisotropy is very strong. Sample Be-E1 has axially symmetric velocity surfaces, similar to the pole figures (Fig. 19). There is strong P-wave anisotropy (>20%) and strong shear-wave splitting, close to 1 km/s for shear-waves passing parallel to the cleavage plane. In sample Ch2a preferred orientation is weaker and stretched out along a girdle (Fig. 19). Like (001) poles of phyllosilicates, velocities show an orthorhombic pattern with highest P-wave velocities parallel to the lineation. Shear-wave splitting is about 600 m/s (Fig. 25).

Since slates and related phyllosilicate-rich rocks such as phyllites and schists are common in continental crustal belts they contribute significantly to seismic anisotropy which should be taken into account in seismic surveys (e.g. Christensen and Mooney, 1965; Cholach and Schmitt, 2006).

Interestingly the seismic anisotropy of slates, as displayed in Fig. 25 is similar to shales, even though shales have much weaker preferred orientation (e.g. Hornby, 1998; Valcke et al., 2006; Vernik and Liu, 1997; Vasin et al., 2013; Kanitpanyacharoen, W., 2015). This can largely be attributed to a significant fraction of oriented porosity in shales which is not observed in slates. Also, the volume fraction of quartz in shales is generally lower.

#### 8.9. Different methods to measure textures

In this review we have compared determinations of crystal preferred orientation using different methods. The preferred orientation in slates demonstrates that high energy X-ray diffraction ( $\lambda \sim 0.1 \text{ \AA}$ ) is an efficient method for quantitative texture analysis of fine-grained multiphase rocks with strong preferred orientation. Some details will need to be improved in the future such as smaller integration increments for images and a finer ODF grid for the Rietveld refinement. Experiments are very fast, less than 20 min per sample, and this could even be improved by developing automatic sample changers. It would be interesting to compare synchrotron X-ray results with high resolution EBSD on the same samples. Notice that the texture strength of phyllosilicates based on high energy X-rays and EBSD is much higher than that based on conventional pole figure goniometry (10–20 mrd) and thus – if the March model would apply to slates – strains would have been greatly underestimated.

For synchrotron diffraction analysis there are also limitations. Especially for extreme preferred orientation. In this study azimuthal segments of diffraction images were integrated over  $10^\circ$ , diffraction images were recorded in  $15^\circ$  increments, ODF resolution in the MAUD Rietveld refinement was  $7.5^\circ$ . This limits the resolution of the texture refinement and the real texture strength may be considerably higher. The diffraction images in Fig. 13 are all of samples with strong textures but you notice that even for Be-E1 (Fig. 13a) the diffraction ring Ch002, for example, displays also some intensities perpendicular to the foliation. In (001) pole figures (Fig. 19) this is expressed by minimum intensities, which are not zero (Table 2). Another artifact could be produced in the Rietveld refinement, since the quartz 101 diffraction is superposed on the muscovite 006 diffraction (Fig. 14 and Fig. SM 1). To avoid this complication the region containing these peaks ( $20.1.6^\circ\text{--}1.8^\circ$ ) has been excluded in some refinements (the overlap could cause both an exaggerated texture for quartz and a high background component for muscovite). In future studies such factors should be taken into account.

While X-ray diffraction averages over the whole sample volume, EBSD records orientations of individual crystals that were indexed and does not record very fine-grained components, thus the value of the lowest pole densities is lower for EBSD than for X-ray diffraction. Some local pole densities may be artificially high due to large grain size, e.g. for (0001) quartz in Fig. 22.

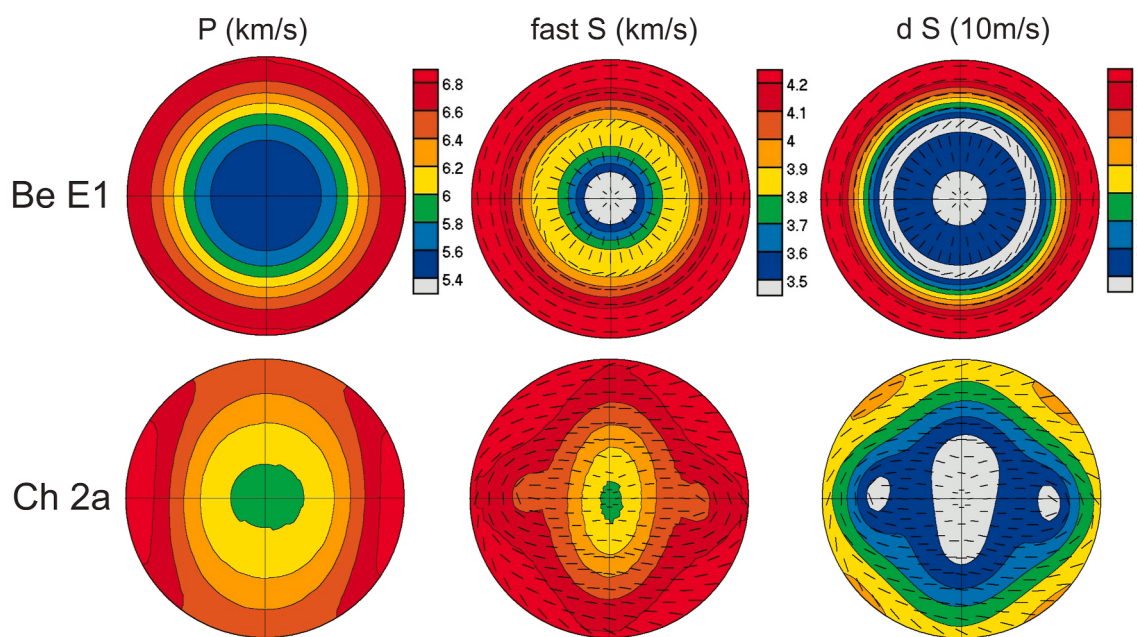


**Fig. 25.** Seismic velocities of slates from the Belgian Ardennes (Be-E1) and China (Ch2a), based on composition and preferred orientation. Equal area projection on the cleavage plane. For S-waves the polarization direction of the fast S-wave is indicated.

## 9. Conclusions

Slates have an extraordinary cleavage and because of this have been used as tiles since Prehistoric times. The cleavage is caused by preferred orientation of phyllosilicates. Early CPO studies investigated preferred orientation with pole figure goniometry. Since then new methods such as high energy synchrotron X-ray diffraction and EBSD gave striking evidence of even stronger phyllosilicate preferred orientation. Crystallites in these fine-grained multiphase rocks are aligned even more perfectly than in highly deformed metals. Equally surprising is the virtual absence of preferred orientation in highly flattened quartz. This can best be attributed to growth and dissolution at relatively low-grade metamorphic conditions. The alignment of phyllosilicates produces strong anisotropy of elastic properties, relevant to seismic wave propagation. In the future the same techniques should be applied to systematic studies of exploring the transition regimes between shale and slate during diagenesis, as well as slate and schist during progressive metamorphism.

## Declaration of competing interest

The authors of this review have no conflict of interest related to this publication which is purely academic, with no external obligations. The research has been supported by Federal agencies as specified in the acknowledgements.

## Acknowledgments

We are obliged to Timothy Horscroft for inviting us to prepare this review. We acknowledged access to beamline 11-ID-C of the Advanced Photon Source (APS), Argonne National Laboratory, supported by DOE Office of Science under Contract No. DE-AC02-06CH11357 and the Zeiss EVO SEM at EPS, UC Berkeley. Yang Ren helped with APS experiments and Tim Teague helped with sample preparation as well as SEM and XRD analyses. Luca Lutterotti, Mauro Bortolotti and Roman Vasin helped with the Rietveld refinement. HRW is appreciative for support from NSF (EAR 1343908) and DOE (DE-FG02-05ER15637) and from The Fulbright Foundation for a fellowship in Salamanca. RY acknowledges support from IKSTP, Shaanxi, China (No. 2015GY101). VC is grateful to his grant PA-18-ACB17-11, from the Program Marie -Curie funded COFUND by the Government of Asturias (Spain) and the Spanish FICYT. MALS was supported by the European Union and the Government of the Principality of Asturias through the “Clarín-Cofund” program [grant number ACA17-32] within the Marie Skłodowska-Curie COFUND (FP7) Actions. We appreciate receiving samples from Juan Gomez Barreiro (Salamanca) and David Lawler (Grass Valley CA). We are greatly indebted to two reviewers, Rob Knipe and Ben van der Plujim, as well as the editor Joao Hippert for their detailed comments that helped to improve the manuscript. HRW is grateful to all the contributions from his co-authors, particularly to Rong Yu for her meticulous analytical work.

## Appendix A. Supplementary data

Supplementary data to this article can be found online at <https://doi.org/10.1016/j.jsg.2020.104066>.

## References

- Alam, M.R., Swamidas, A.S.J., Gale, J., Munaswamy, K., 2008. Mechanical and physical properties of slate from britannia cove, newfoundland. *Can. J. Civ. Eng.* 35 (7), 751–755. <https://doi.org/10.1139/L08-042>.
- Asselberghs, E., 1924. Les ardoisières du Dévonien de l'Ardenne. *Annales des Mines de Belgique*, pp. 1037–1098.
- Attewell, P.B., Taylor, R.K., 1969. A microtextural interpretation of a welsh slate. *Int. J. Rock Mech. Min. Sci.* 6, 423–438. [https://doi.org/10.1016/0148-9062\(69\)90011-4](https://doi.org/10.1016/0148-9062(69)90011-4).
- Biedermann, A.R., Koch, C.B., Lorenz A., W.E., Hirt, A.M., 2014. Low temperature magnetic anisotropy in micas and chlorite. *Tectonophysics* 629, 63–74. <https://doi.org/10.1016/j.tecto.2014.01.015>.
- Bogen, N.L., 1984. Stratigraphy and sedimentary petrology of the upper jurassic Mariposa formation, western Sierra Nevada, California. In: Croach, J.K., Bachman, S. B. (Eds.), *Tectonics and Sedimentation along the California Margin*. Pacific Section S. E.P.M. vol. 38, pp. 119–134.
- Borradaile, G.J., Henry, B., 1997. Tectonic applications of magnetic susceptibility and its anisotropy. *Earth Sci. Rev.* 42, 49–93. [https://doi.org/10.1016/S0012-8252\(96\)00044-X](https://doi.org/10.1016/S0012-8252(96)00044-X).
- Borradaile, G.J., Jackson, M., 2010. Structural geology, petrofabrics and magnetic fabrics (AMS, AARM, AIRM). *J. Struct. Geol.* 32, 1519–1551. <https://doi.org/10.1016/j.jsg.2009.09.006>.
- Brandolini, P., 1988. L'utilizzazione dell'ardesia in Liguria. *Studi e ricerche di Geografia* 11, 31–85.
- Briggs, D.E.G., Raiswell, R., Bottrell, S.H., Hatfield, D., Bartels, C., 1996. Controls on the pyritization of exceptionally preserved fossils: an analysis of the Lower Devonian Hunsrück slate of Germany. *Am. J. Sci.* 296, 633–663. <https://doi.org/10.2475/ajs.296.6.633>.
- Cárdenes, V., Cnudde, V., Cnudde, J.P., 2014. Iberian roofing slate as a global heritage stone Province resource. *Episodes* 38 (2), 97–105.
- Cárdenes, V., Ponce de León, M., Rodríguez, X.A., Rubio-Ordoñez, A., 2019. Roofing slate industry in Spain: history, geology, and geoheritage. *Geoheritage* 11 (1), 19–34. <https://doi.org/10.1007/s12371-017-0263-y>.
- Chernicoff, C.J., Zappettini, E.O., Santos, J.O.S., Beyer, E., McNaughton, N.J., 2008. Foreland basin deposits associated with Cuyania accretion in La Pampa Province, Argentina. *Gondwana Res.* 13 (2), 189–203. <https://doi.org/10.1016/j.gr.2007.04.006>.
- Cholach, P.Y., Schmitt, D.R., 2006. Intrinsic elasticity of a textured phyllosilicate aggregate: relation to the seismic anisotropy of shales and schists. *J. Geophys. Res.* 111, B09410 <https://doi.org/10.1029/2005JB004158>.
- Christensen, N.I., 1965. Compressional wave velocities in metamorphic rocks at pressures to 10 kbar. *J. Geophys. Res.* 70, 6147–6164. <https://doi.org/10.1029/JZ070i024p06147>.
- Christensen, N.I., Mooney, W.D., 1965. Seismic velocity structure and composition of the continental crust: a global view. *J. Geophys. Res.* 100, 9761–9788. <https://doi.org/10.1029/95JB00259>.
- Clark, L.D., 1964. *Stratigraphy and Structure of Part of the Western Sierra Nevada Metamorphic Belt, California*, vol. 410. U.S. Geol. Survey Professional Paper, p. 70.
- Clark, B.R., 1970. Mechanical formation of preferred orientation in clays. *Am. J. Sci.* 269 (3), 250–266. <https://doi.org/10.2475/ajs.269.3.250>.
- Cnudde, J.P., 1998. History of the Belgian slate industry. Homologation and sampling of natural stone in Belgium. The part of the Applied Geology Laboratory of the University of Gent in the homologation and the choice of natural stones. *Naturwetenschappelijk Tijdschr.* 78 (1–4), 13–20.
- Cornelius, H.P., 1950. *Geologie der Err.-Julier-Gruppe. II. Teil: der gebirgsbau. Beitr. Geol. Karte Schweiz [N.F.] 70/72*.
- Cosgrove, J.W., 1976. The formation of crenulation cleavage. *J. Geol. Soc.* 132, 155–178. <https://doi.org/10.1144/gsjgs.132.2.0155>.
- Davies, D.C., 1878. *A Treatise on Slate and Slate Quarrying*. Crosby, London, p. 186pp.
- Day, H.W., Moores, E.M., Tuminas, A.C., 1985. Structure and tectonics of the northern Sierra Nevada. *Geol. Soc. Am. Bull.* 96, 436–450. [https://doi.org/10.1130/0016-7606\(1985\)96%3C436:SATOTN%3E2.0.CO;2](https://doi.org/10.1130/0016-7606(1985)96%3C436:SATOTN%3E2.0.CO;2).
- De Boer, R.B., 1977. Pressure solution: theory and experiments. *Tectonophysics* 39, 287–301. [https://doi.org/10.1016/0040-1901\(77\)90101-9](https://doi.org/10.1016/0040-1901(77)90101-9).
- De Clercq, W., 2011. Roman rural settlements in Flanders. Perspectives on a ‘non-villa’ landscape in extrema Galliarum. In: Roymans, N., Derkx, T. (Eds.), *Villa Landscapes in the Roman North*. Amsterdam University Press Amsterdam, pp. 235–257.
- Del Soldato, M., Coli, M., 2013. L'ardesia della Val Lavagna: pietra del paesaggio e della cultura. In: 5° Congresso Nazionale Geologia e Turismo, Bologna.
- Dieterich, J.H., 1969. Origin of slaty cleavage in folded rocks. *Am. J. Sci.* 267, 155–165. <https://doi.org/10.2475/ajs.267.2.155>.
- Durney, D.W., 1972. Solution transfer, an important geological deformation mechanism. *Nature* 235, 315–317. <https://doi.org/10.1038/235315a0>.
- Engelder, T., Geiser, P., 1979. The relationship between pencil cleavage and lateral shortening within the Devonian section of the Appalachian Plateau, New York. *Geology* 7, 460–464. [https://doi.org/10.1130/0091-7613\(1979\)7%3C460:TRBCPA%3E2.0.CO;2](https://doi.org/10.1130/0091-7613(1979)7%3C460:TRBCPA%3E2.0.CO;2).
- Eric, J.H., Stromquist, A.A., Swinney, C.M., 1955. Geology and mineral deposits of the Angels Camp and Sonora quadrangles, Calaveras and Tuolumne Counties, California. *Cal. Div. Mines and Geology. Special Report* 41, 55pp.
- Fazio, E., Punturo, R., Cirrincione, R., Kern, H., Pezzino, A., Wenk, H.-R., Goswami, S., Mamiani, M.A., 2017. Quartz preferred orientation in naturally deformed mylonitic rocks (Montalto Shear Zone – Italy): a comparison of results by different techniques, their advantages and limitations. *Int. J. Earth Sciences* 106, 2259–2278. <https://doi.org/10.1007/s00531-016-1424-y>.
- Fieltz, W., 1992. Variscan transpressive inversion in the northwestern central Rhenohercynian belt of western Germany. *J. Struct. Geol.* 14 (5), 547–563. [https://doi.org/10.1016/0191-8141\(92\)90156-Q](https://doi.org/10.1016/0191-8141(92)90156-Q).
- Fossen, H., 2016. *Structural Geology*, second ed. Cambridge University Press. ISBN-978-1107057647.
- García-Guinea, J., Lombardero, M., Roberts, B., Taboada, J., 1997. Spanish roofing slate deposits. *Trans. Inst. Miner. Metall. Sect. B* 106, 205–214.
- García-Guinea, J., Lombardero, M., Roberts, B., Peto, A., 1998. Mineralogy and microstructure of roofing slate: thermo-optical behaviour and fissility. *Mater. Constr.* 48 (251), 37–48.

- Godfrey, N.J., Christensen, N.I., Okaya, D.A., 2000. Anisotropy of schists: contribution of crustal anisotropy to active source seismic experiments and shear wave splitting observations. *J. Geophys. Res.* 105 (B12), 27991–28007. <https://doi.org/10.1029/2000JB900286>.
- Gray, D.R., 1977. Some parameters which effect the morphology of crenulation cleavage. *J. Geol.* 85, 763–780.
- Gray, D.R., Durney, D.W., 1979. Crenulation cleavage differentiation: implications of solution-deposition processes. *J. Struct. Geol.* 1, 73–80. [https://doi.org/10.1016/0191-8141\(79\)90023-3](https://doi.org/10.1016/0191-8141(79)90023-3).
- Gwyn, D., 2015. Welsh Slate: Archaeology and History of an Industry. Royal Commission on the Ancient and Historical Monuments of Wales. ISBN-10: 1871184517.
- Haerinck, T., Adriaens, R., Debacker, T.N., Hirt, A.M., Sintubin, M., 2013. Paramagnetic metamorphic mineral assemblages controlling AMS in low-grade deformed metasediments and the implications with respect to the use of AMS as a strain marker. *London J. Geol. Soc.* 170, 263–280. <https://doi.org/10.1144/jgs2012-062>.
- Haerinck, T., Wenk, H.-R., Debacker, T.N., Sintubin, M., 2015. Preferred mineral orientation of a chloritoid-bearing slate in relation to its magnetic fabric. *J. Struct. Geol.* 71, 125–135. <https://doi.org/10.1016/j.jsg.2014.09.013>.
- Handy, M.R., Herwegen, M., Kamber, B.S., Tietz, R., Villa, I.M., 1996. Geochronologic, petrologic and kinematic constraints on the evolution of the Err-Platta boundary, part of a fossil continent-ocean suture in the Alps (eastern Switzerland). *Schweiz. Mineral. Petrogr. Mitt.* 76, 453–474.
- Heyliger, P., Ledbetter, H., Kim, S., 2002. Elastic constants of natural quartz. *J. Acoust. Soc. Am.* 114, 644–650. <https://doi.org/10.1121/1.1593063>.
- Hielscher, R., Schaeben, H., 2008. A novel pole figure inversion method: specification of the MTEX algorithm. *J. Appl. Crystallogr.* 41, 1024–1037. <https://doi.org/10.1107/S0021889808030112>.
- Ho, N.-C., Peacor, D.R., van der Pluijm, B.A., 1995. Reorientation mechanisms of phyllosilicates in the mudstone-to-slate transition at Lehigh Gap, Pennsylvania. *J. Struct. Geol.* 17, 345–356. [https://doi.org/10.1016/0191-8141\(94\)00065-8](https://doi.org/10.1016/0191-8141(94)00065-8).
- Ho, N.-C., Peacor, D.R., van der Pluijm, B.A., 1996. Contrasting roles of detrital and authigenic phyllosilicates during slaty cleavage development. *J. Struct. Geol.* 18, 615–623. [https://doi.org/10.1016/S0191-8141\(96\)80028-9](https://doi.org/10.1016/S0191-8141(96)80028-9).
- Ho, N.-C., van der Pluijm, B.A., Peacor, D.R., 2001. Static recrystallization and preferred orientation of phyllosilicates: Michigamme Formation, northern Michigan, USA. *J. Struct. Geol.* 23, 887–893. [https://doi.org/10.1016/S0191-8141\(00\)00162-0](https://doi.org/10.1016/S0191-8141(00)00162-0).
- Hornby, B.E., 1998. Experimental laboratory determination of the dynamic elastic properties of wet, drained shales. *J. Geophys. Res.* 103, 29945–29964. <https://doi.org/10.1029/97JB02380>.
- Housen, B.A., Richter, C., van der Pluijm, B.A., 1993. Composite magnetic anisotropy fabrics: experiments, numerical models, and implications for the quantification of rock fabrics. *Tectonophysics* 220, 1–12. [https://doi.org/10.1016/0040-1951\(93\)90219-A](https://doi.org/10.1016/0040-1951(93)90219-A).
- Hughes, T., Horak, J., Lott, G., Roberts, D., 2016. Cambrian age Welsh Slate: a global heritage stone resource from the United Kingdom. *Episodes* 39 (1), 45–52. <https://doi.org/10.18814/epiugs/2016/v39i1/89236>.
- Hutchinson, W.B., Nes, E., 1992. Texture development during grain growth – a useful rule-of-thumb. *Proc. Grain Growth in Polycrystalline Materials I. Mater. Sci. Forum* 94–96, 385–390.
- Iglesias Ponce de León, M., 1995. L'ardoise en Espagne: Histoire et économie, vol. 2. Université de Rennes, Rennes.
- Ishii, K., 1988. Grain growth and re-orientation of phyllosilicate minerals during the development of slaty cleavage in the South Kitakami Mountains, northeast Japan. *J. Struct. Geol.* 10, 145–154. [https://doi.org/10.1016/0191-8141\(88\)90112-5](https://doi.org/10.1016/0191-8141(88)90112-5).
- Jeffery, G.B., 1923. The motion of ellipsoidal particles immersed in a viscous fluid. *Proc. Roy. Soc. Lond.* 102, 161–179.
- Jinbiao, S., 2010. The characteristics of black roofing slate deposit in Western Hubei. *Chin. Non-metallic Min. Ind. Her.* 2, 52–53.
- Jope, E.M., Dunning, G.C., 2011. The use of blue slate for roofing in medieval England. *Antiq. J.* 34 (3–4), 209–217. <https://doi.org/10.1017/s0003581500059886>.
- Kamb, W.B., 1959. Theory of preferred crystal orientation developed by crystallization under stress. *J. Geol.* 67, 153–170.
- Kanitpanyacharoen, W., Kets, F.B., Wenk, H.-R., Wirth, R., 2012. Preferred orientation, microstructures and porosity analyses of Posidonia shales. *Clay Clay Miner.* 60, 315–329. <https://doi.org/10.1346/CCMN.2012.0600308>.
- Klein, H., Hielscher, R., Schaeben, H., 2010. Texture analysis with MTEX – free and open software toolbox. *Solid State Phenom.* 160, 63–68. <https://doi.org/10.4028/www.scientific.net/SSP.160.63>.
- Knipe, R.J., 1979. Chemical changes during slaty cleavage development. *Bull. Mineral.* 102, 206–209.
- Knipe, R.J., 1981. The interaction of deformation and metamorphism in slates. *Tectonophysics* 78, 249–272. [https://doi.org/10.1016/0040-1951\(81\)90016-0](https://doi.org/10.1016/0040-1951(81)90016-0).
- Knipe, R.J., White, S.H., 1977. Microstructural variation of an axial plane cleavage around a fold. A H.V.E.M. study. *Tectonophysics* 39, 355–381. [https://doi.org/10.1016/0040-1951\(77\)90104-4](https://doi.org/10.1016/0040-1951(77)90104-4).
- Kocks, U.F., Tomé, C., Wenk, H.-R., 2000. Texture and Anisotropy. Preferred Orientations in Polycrystals and Their Effect on Materials Properties, 2nd paperback edition. Cambridge University Press. 676pp, ISBN 0521-4651-8.
- Large, D.J., Christy, A.G., Fallick, A.E., 1994. Poorly crystalline carbonaceous matter in high grade metasediments: implications for graphitisation and metamorphic fluid composition. *Contrib. Mineral. Petrog.* 116, 108–116. <https://doi.org/10.1007/BF00310693>.
- Le Gall, B., 1992. The deep structure of the Ardennes Variscan thrust belt from structural and ECORS seismic data. *J. Struct. Geol.* 14, 531–546. [https://doi.org/10.1016/0191-8141\(92\)90155-P](https://doi.org/10.1016/0191-8141(92)90155-P).
- Lee, J.H., Peacor, D.R., Lewis, D.D., Wintsch, R.P., 1986. Evidence for syntectonic crystallization for the mudstone to slate transition at Lehigh Gap, Pennsylvania, USA. *J. Struct. Geol.* 8, 767–780. [https://doi.org/10.1016/0191-8141\(86\)90024-6](https://doi.org/10.1016/0191-8141(86)90024-6).
- Lindsay, J., 1974. A History of the North Wales Slate Industry. David and Charles, Newton Abbott, ISBN 0-7153 6264-X.
- Lonardelli, I., Wenk, H.-R., Ren, Y., 2007. Preferred orientation and elastic anisotropy in shales. *Geophysics* 72, D33–D40. <https://doi.org/10.1190/1.2435966>.
- Lutterotti, L., Matthies, S., Wenk, H.-R., Schultz, A.J., Richardson, J.W., 1997. Combined texture and structure analysis of deformed limestone from time-of-flight neutron diffraction spectra. *J. Appl. Phys.* 81, 594–600. <https://doi.org/10.1063/1.364220>.
- Lutterotti, L., Vasin, R., Wenk, H.-R., 2014. Rietveld texture analysis from synchrotron diffraction images. I. Calibration and basic analysis. *Powder Diffr.* 29, 76–84. <https://doi.org/10.1017/S0885715613001346>.
- March, A., 1932. Mathematische Theorie der Regelung nach der Korngestalt bei affiner Deformation. *Z. Kristallogr.* 81, 285–297.
- Martin-Hernandez, E., Hirt, A.M., 2003. The anisotropy of magnetic susceptibility in biotite, muscovite and chlorite single crystals. *Tectonophysics* 367, 13–28. [https://doi.org/10.1016/S0040-1951\(03\)00127-6](https://doi.org/10.1016/S0040-1951(03)00127-6).
- Matthies, S., Wenk, H.-R., 2009. Transformations for monoclinic crystal symmetry in texture analysis. *J. Appl. Crystallogr.* 42, 564–571. <https://doi.org/10.1107/S0021889809018172>.
- McWhirr, A., 1988. The Roman Swithland slate industry. *Trans. Leics. Archaeol. Hist. Soc.* 62, 1–8.
- Means, W.D., 1981. The concept of steady-state foliation. *Tectonophysics* 78 (1–4), 179–199. [https://doi.org/10.1016/0040-1951\(81\)90013-5](https://doi.org/10.1016/0040-1951(81)90013-5).
- Means, W.D., Paterson, M.S., 1966. Experiments on preferred orientation of platy minerals. *Contrib. Mineral. Petrol.* 13 (2), 108–133. <https://doi.org/10.1007/BF00518022>.
- Merriman, R.J., Roberts, B., Peacor, D.R., 1990. A transmission electron microscope study of white mica crystallite size distribution in a mudstone to slate transitional sequence. *Contrib. Mineral. Petrol.* 106, 27–40. <https://doi.org/10.1007/BF00306406>.
- Morris, A.P., 1981. Competing deformation mechanisms and slaty cleavage in deformed, quartzose meta-sediments. *J. Geol. Soc. London* 138 (4), 455–462. <https://doi.org/10.1144/gsjgs.138.4.0455>.
- Mukhopadhyay, D., 1973. Strain measurements from deformed quartz grains in slaty rocks from the Ardennes and the northern Eifel. *Tectonophysics* 16 (3–4), 279–296. [https://doi.org/10.1016/0040-1951\(73\)90016-4](https://doi.org/10.1016/0040-1951(73)90016-4).
- Oertel, G., 1970. Deformation of a slaty, lapillar tuff in the Lake District, England. *Geol. Soc. Am. Bull.* 81, 1173–1188. [https://doi.org/10.1130/0016-7606\(1970\)81\[1173:DOASLT\]2.0.CO;2](https://doi.org/10.1130/0016-7606(1970)81[1173:DOASLT]2.0.CO;2).
- Oertel, G., 1983. The relationship of strain and preferred orientation of phyllosilicate grains in rocks—a review. *Tectonophysics* 100, 413–447. [https://doi.org/10.1016/0040-1951\(83\)90197-X](https://doi.org/10.1016/0040-1951(83)90197-X).
- Oertel, G., Curtis, C.D., 1972. Clay ironstone concretion preserving fabrics due to progressive compaction. *Geol. Soc. Am. Bull.* 83, 2597–2606. [https://doi.org/10.1130/0016-7606\(1972\)83\[2597:CCPDT\]2.0.CO;2](https://doi.org/10.1130/0016-7606(1972)83[2597:CCPDT]2.0.CO;2).
- Oertel, G., Phakey, P.P., 1972. The texture of a slate from nantlle, caernarvon, North Wales. *Texture* 1, 1–8. <https://doi.org/10.1155/TSM.1.1>.
- Oertel, G., Curtis, C.D., Phakey, P.P., 1973. A transmission electron microscope and x-ray diffraction study of muscovite and chlorite. *Mineralog. Mag.* 39, 176–188. <https://doi.org/10.1180/minmag.1973.039.302.05>.
- Oncken, O., Plesch, A., Weber, J., Ricken, W., Schrader, S., 2000. Passive margin detachment during arc-continent collision (Central European Variscides). In: Franke, W., Haak, V., Oncken, O., Tanner, D. (Eds.), *Orogenic Processes: Quantification and Modelling in the Variscan Belt*, vol. 179. Geological Society, London, Special Publications, pp. 199–216.
- Ortleva, P., Merino, E., Strickholm, P., 1982. Kinetics of metamorphic layering in anisotropically stressed rocks. *Am. J. Sci.* 282, 617–643. <https://doi.org/10.2475/ajs.282.5.617>.
- Passchier, C.W., Trouw, R.A.J., 2005. *Microtectonics*, second ed. Springer-Verlag. ISBN 3-540-64003-7.
- Paterson, M.S., 1973. Nonhydrostatic thermodynamics and its geologic applications. *Rev. Geophys. Space Phys.* 11–2, 355–389.
- Paterson, M.S., Weiss, L.E., 1966. Experimental deformation and folding in phyllite. *Geol. Soc. Am. Bull.* 77, 343–374. [https://doi.org/10.1130/0016-7606\(1966\)77\[343:EDAFIP\]2.0.CO;2](https://doi.org/10.1130/0016-7606(1966)77[343:EDAFIP]2.0.CO;2).
- Pehl, J., Wenk, H.-R., 2005. Evidence for regional Dauphiné twinning in quartz from the Santa Rosa mylonite zone in Southern California. A neutron diffraction study. *J. Struct. Geol.* 27, 1741–1749. <https://doi.org/10.10107/S0021889805006059>.
- Ponce de Leon, M., 2012. L'ardoise en Espagne. De la Préhistoire aux Hispano-Romains. In: Marchand, G., Querre, G. (Eds.), *Roches et Sociétés de la Préhistoire*. Presses Universitaires de Rennes, pp. 351–375.
- Powell, C.McA., 1972. Tectonic dewatering and strain in the Michigamme slate, Michigan. *Geol. Soc. Am. Bull.* 83, 2149–2158. [https://doi.org/10.1130/0016-7606\(1972\)83\[2149:TDAST\]2.0.CO;2](https://doi.org/10.1130/0016-7606(1972)83[2149:TDAST]2.0.CO;2).
- Price, W.R., Ronck, C.L., 2019. Quarrying for world heritage designation: slate tourism in North Wales. *Geoheritage*. <https://doi.org/10.1007/s12371-019-00402-0>.
- Raiswell, R., Newton, R.J., Bottrell, S.H., Coburn, P.M., Briggs, D.E.G., Bond, D.P.G., Poulton, S.W., 2008. Turbidite depositional influences on the diagenesis of Beecher's Trilobite Bed and the Hunsrück Slate; sites of soft tissue pyritization. *Am. J. Sci.* 308, 105–129. <https://doi.org/10.2475/02.2008.01>.
- Ramsay, J.G., Huber, M.J., 1983. *Strain Analysis*. In: *The Techniques of Modern Structural Geology*, Vol. 1: *Strain Analysis*. Academic Press, London. ISBN 978-0125769211.

- Ratcliffe, N.M., Stanley, R.S., Gale, M.H., Thompson, P.J., Walsh, G.J., 2011. Bedrock Geologic Map of Vermont. U.S. Geological Survey Scientific Investigations Map 3184, 3 Sheets, Scale 1:100,000. U.S. Geological Survey.
- Reed, S.J.B., 2010. Electron Microprobe Analysis and Scanning Electron Microscopy in Geology, second ed. Cambridge University Press <https://doi.org/10.1017/CBO9780511610561>.
- Richards, A.J., 2007. Welsh Slate Craft. A Brief Account of Welsh Slate Working. Gwasg Carreg Gwalch. ASIN: B01N9N90TQ.
- Rietveld, H.M., 1969. A profile refinement method for nuclear and magnetic structures. *J. Appl. Crystallogr.* 2, 65–71. <https://doi.org/10.1107/S0021889869006558>.
- Robinson, D., 1971. The inhibiting effect of organic carbon on contact metamorphic recrystallization of limestones. *Contrib. Mineral. Petro.* 32, 245–250. <https://doi.org/10.1007/BF00373342>.
- Rutter, E.H., 1976. The kinetics of rock deformation by pressure solution. *Phil Trans. Roy. Soc. London A* 283, 203–219. <https://doi.org/10.1098/rsta.1976.0079>.
- Sander, B., 1950. Einführung in die Gefügekunde der Geologischen Körper, Zweiter Teil: die Körnigefüge. Springer Verlag, Wien.
- Sander, B., Sachs, G., 1930. Zur röntgenoptischen gefügeanalyse von Gesteinen. *Z. Kristallogr.* 75 (5,6), 550–571.
- Schavemaker, Y.A., de Bresser, J.H.P., Van Baelen, H., Sintubin, M., 2012. Geometry and kinematics of the low-grade metamorphic 'Herbeumont shear zone' in the High-Ardennes slate belt (Belgium). *Geol. Belg.* 15, 126–136.
- Schmidt, W., 1925. Gefügestatistik. *Tschermaks Mineral. Petrog. Mitt.* 38, 392–423.
- Sharma, A.K., Sharma, R., Dandi, H.R., 2019. Mineral Resources of Himachal Pradesh. Department of Industries of Udyog Bhawan, p. 134.
- Shimizu, I., 1992. Nonhydrostatic and nonequilibrium thermodynamics of deformable materials. *J. Geophys. Res.* 97 (B4), 4587–4597. <https://doi.org/10.1029/91JB02859>.
- Siddans, A.W.B., 1972. Slaty cleavage: a review of research since 1815. *Earth Sci. Rev.* 8 (2), 205–212.
- Siddans, A.W.B., 1976. A discussion on natural strain and geological structure - Deformed rocks and their textures. *Phil. Trans. Roy. Soc. Lond.* 283, 43–54. <https://doi.org/10.1098/rsta.1976.0068>.
- Sintubin, M., 1993. The phyllosilicate texture as a strain marker in structural geology. *Mater. Sci. Forum* 133–136, 769–776.
- Sintubin, M., 1994a. Phyllosilicate preferred orientation in relation to strain path determination in the lower Paleozoic Stavelot-Venn Massif (Ardennes, Belgium). *Tectonophysics* 237, 215–231. [https://doi.org/10.1016/0040-1951\(94\)90256-9](https://doi.org/10.1016/0040-1951(94)90256-9).
- Sintubin, M., 1994b. Clay fabrics in relation to the burial history of shales. *Sedimentology* 41, 1161–1169. <https://doi.org/10.1111/j.1365-3091.1994.tb01447.x>.
- Sintubin, M., 1996. Quantitative approach of the cleavage evolution in the dinant allochthon (Ardennes, France – Belgium). *Ann. Soc. Geol. Belg.* 119, 145–158.
- Sintubin, M., 1998. Mica (110) Pole figures in support of Marchian behaviour of phyllosilicates during the development of phyllosilicate preferred orientation. *Mater. Sci. Forum* 273–275, 601–606.
- Snow, C.A., Scherer, H., 2006. Terranes of the Western Sierra Nevada foothills metamorphic belt, California: a critical review. *Int. Geol. Rev.* 48, 46–62. <https://doi.org/10.2747/0020-6814.48.1.46>.
- Sorby, H.C., 1853. On the origin of slaty cleavage. *New Philos. J. (Edinburgh)* 55, 137–148.
- Sorby, H.C., 1856. On the theory of the origin of slaty cleavage. *Phil. Mag.* 12, 127–129.
- Sprunt, E.S., Nur, A., 1977. Experimental studies of the effects of stress on solution rate. *J. Geophys. Res.* 82, 3013–3022. <https://doi.org/10.1029/JB082i020p03013>.
- Stearns, B., Stearns, A., Meyer, J., 2000. Slate roofing and grading in the new millennium. *Interface* 14–16. January 2000.
- Taylor, G.H., Liu, S.Y., Teichmueller, M., 1991. Bituminite – a TEM view. *Int. J. Coal Geol.* 18, 71–85. [https://doi.org/10.1016/0166-5162\(91\)90044-J](https://doi.org/10.1016/0166-5162(91)90044-J).
- Tullis, T.E., 1976. Experiments on the origin of slaty cleavage and schistosity. *Geol. Soc. Am. Bull.* 87, 745–753. [https://doi.org/10.1130/0016-7606\(1976\)87%3C745:EOTOQS%3E2.0.CO;2](https://doi.org/10.1130/0016-7606(1976)87%3C745:EOTOQS%3E2.0.CO;2).
- Tullis, T.E., Wood, D.S., 1975. Correlation of finite strain from both reduction bodies and preferred orientation of mica in slate from Wales. *Geol. Soc. Am. Bull.* 86, 632–638. [https://doi.org/10.1130/0016-7606\(1975\)86%3C632:COFSFB%3E2.0.CO;2](https://doi.org/10.1130/0016-7606(1975)86%3C632:COFSFB%3E2.0.CO;2).
- Twiss, J.J., Moores, E.M., 2006. Structural Geology, second ed. W.H. Freeman. ISBN 0 7167 2252.
- Valcke, S.L.A., Casey, M., Lloyd, G.E., Kendall, J.-M., Fisher, Q.J., 2006. Lattice preferred orientation and seismic anisotropy in sedimentary rocks. *Geophys. J. Int.* 166, 652–666. <https://doi.org/10.1111/j.1365-246X.2006.02987.x>.
- van der Pluijm, B.A., Ho, N.-C., Peacor, D.R., Merriman, R.J., 1998. Contradictions of slate formation resolved? *Nature* 392, 348. <https://doi.org/10.1038/32810>.
- Van Noorden, M., Sintubin, M., Darboux, J.-R., 2007. Incipient strain partitioning in a slate belt: evidence from the early Variscan Monts d'Arrée slate belt (Brittany, France). *J. Struct. Geol.* 29, 837–849. <https://doi.org/10.1016/j.jsg.2007.01.002>.
- Van Noten, K., Hilgers, C., Urai, J., Sintubin, M., 2012. The complexity of 3D stress-state changes during compressional tectonic inversion at the onset of orogeny. In: Healy, et al. (Eds.), Faulting, Fracturing, and Igneous Intrusion in the Earth's Crust, vol. 367. *Geol. Soc. London Spec. Publ.*, pp. 51–69. <https://doi.org/10.1144/SP367.5>.
- Wenck, R., Wenk, H.-R., Kanitpanyacharoen, W., Matthies, S., Wirth, R., 2013. Anisotropy of Kimmeridge shale. *J. Geophys. Res.* 118, 1–26. <https://doi.org/10.1002/jgrb.50259>.
- Wenck, R., Kern, H., Lokajicek, T., Svitek, T., Lehmann, E., Mannes, D.C., Chaouche, M., Wenk, H.-R., 2017. Elastic anisotropy of Tambo gneiss from Promontogno, Switzerland: a comparison of crystal orientation and microstructure-based modeling and experimental measurements. *Geophys. J. Int.* 209, 1–20. <https://doi.org/10.1093/gji/ggw487>.
- Vaughan, M.T., Guggenheim, S., 1986. Elasticity of muscovite and its relationship to crystal structure. *J. Geophys. Res.* 91, 4657–4664. <https://doi.org/10.1029/JB091iB05p04657>.
- Vernik, L., Liu, X., 1997. Velocity anisotropy in shales: a petrophysical study. *Geophysics* 62, 521–532. <https://doi.org/10.1190/1.1444162>.
- Voisin, L., 1987. Les Ardoisières de l'Ardenne. Editions Terres Ardennaises, Charleville-Mézières (La Fortelle).
- Voltolini, M., Wenk, H.-R., Mondol, N.H., Bjørlykke, K., Jahren, J., 2009. Anisotropy of experimentally compressed kaolinite-ilomite-quartz mixtures. *Geophysics* 74, D13–D23. <https://doi.org/10.1190/1.3002557>.
- Von Gehlen, K., 1960. Die röntgenographische und optische Gefügeanalyse von Erzen, insbesondere mit dem Zählrohr-Texturgoniometer. *Beitr. Mineral. Petrog.* 7, 340–388.
- von Plessmann, W., 1966. Lösung, Verformung, Transport und Gefüge. *Z. Dtsch. Geol. Ges.* 115, 650–663.
- von Plessmann, W., 1964. Gesteinslösung, ein Hauptfaktor beim Schieferungsprozess. *Geol. Mitt. Aachen* 4, 69–82.
- Wagner, H.W., 2014. Geologische Untersuchung und Materialprüfung an Dachschiefer-Altdeckungen. *Mainz. Geowiss. Mitt.* 42, 121–142.
- Wagner, W., Le Bail, R., Hacar, M., Stanek, S., 1995. European roofing slates part 2: geology of selected examples of slates deposits. *Z. Angew. Geol.* 41, 21–26.
- Wagner, H.W., Baumann, H., Negedank, J., Roschig, F., 1997. Geological, petrographic, geochemical and petrophysical investigations on roofing slates. *Mainz. Geowiss. Mitt.* 25, 131–184.
- Wagner, W., Le Bail, R., Hacar, M., Stanek, S., 1994. European roofing slates part 1: remarks to the geology of mineral deposits. *Z. Dtsch. Ges. Geowiss.* 40, 68–74.
- Wallis, D., Lloyd, G.E., Phillips, R.J., Parsons, A.J., Walshaw, R.D., 2015. Low effective fault strength due to frictional-viscous flow in phyllonites, Karakoram Fault Zone, NW India. *J. Struct. Geol.* 77, 45–61. <https://doi.org/10.1016/j.jsg.2015.05.010>.
- Wallis, D., Hansen, L.N., Ben Britton, T., Wilkinson, A.J., 2016. Geometrically necessary dislocation densities in olivine obtained using high-angular resolution electron backscatter diffraction. *Ultramicroscopy* 168, 34–45. <https://doi.org/10.1016/J.ULTRAMIC.2016.06.002>.
- Walsh, J.A., 2007. The use of the scanning electron microscope in the determination of the mineral composition of Ballachulish slate. *Mater. Char.* 58, 1095–1103. <https://doi.org/10.1016/j.matchar.2007.04.013>.
- Ward, C., Gómez-Fernandez, F., 2003. Quantitative mineralogical analysis of Spanish roofing slates using the Rietveld method and X-ray powder diffraction data. *Eur. J. Mineral.* 15, 1051–1062. <https://doi.org/10.1127/0935-1221/2003/0015-1051>.
- Weber, K., 1981. Kinematic and metamorphic aspects of cleavage formation in very low-grade metamorphic slates. *Tectonophysics* 78, 291–306. [https://doi.org/10.1016/0040-1951\(81\)90018-4](https://doi.org/10.1016/0040-1951(81)90018-4).
- Wenk, H.-R., Vasin, R., 2017. Preferred orientation patterns of phyllosilicates in surface clays. *Clay Clay Miner.* 65–5, 329–341. <https://doi.org/10.1346/CCMN.2017.064069>.
- Wenk, H.-R., Matthies, S., Donovan, J., Chateigner, D., 1998. BEARTEX: a Windows-based program system for quantitative texture analysis. *J. Appl. Crystallogr.* 31, 262–269. <https://doi.org/10.1107/S002188989700811X>.
- Wenk, H.-R., Lutterotti, L., Kaercher, P., Kanitpanyacharoen, W., Miyagi, L., Vasin, R., 2014. Rietveld texture analysis from synchrotron diffraction images: II. Complex multiphase materials and diamond anvil cell experiments. *Powder Diffr.* 29, 220–232. <https://doi.org/10.1017/S0885715614000360>.
- Wenk, H.R., Kanitpanyacharoen, W., Voltolini, M., 2010. Preferred orientation of phyllosilicates: comparison of fault gouge, shale and schist. *J. Struct. Geol.* 32, 478–489. <https://doi.org/10.1016/j.jsg.2010.02.003>.
- Wenk, H.-R., Kanitpanyacharoen, W., Ren, Y., 2019. Slate – a new record for crystal preferred orientation. *J. Struct. Geol.* 125 (50 year special issue), 319–324. <https://doi.org/10.1016/j.jsg.2017.12.009>.
- Weyl, P.K., 1959. Pressure solution and force of crystallisation-A phenomenological theory. *J. Geophys. Res.* 64 (11), 2001–2025. <https://doi.org/10.1029/JZ064i011p02001>.
- White, S.H., Knipe, R.J., 1978. Microstructure and cleavage development in selected slates. *Contrib. Mineral. Petrol.* 66 (2), 165–174. <https://doi.org/10.1007/BF00372155>.
- Wickert, J., 2020. Slate as Dimension Stone. Origin, Standards, Properties, Mining and Deposits. Springer Mineralogy, p. 492.
- Williams, P.F., 1972. Relationship between axial plane foliation and strain. *Tectonophysics* 30, 181–196. [https://doi.org/10.1016/0040-1951\(76\)90186-4](https://doi.org/10.1016/0040-1951(76)90186-4).
- Wood, D.S., 1974. Current views of the development of slaty cleavage. *Ann. Rev. Earth Sci.* 2, 1–35.
- Wood, D.S., Oertel, G., 1980. Deformation in the cambrian slate belt of Wales. *J. Geol.* 88 (3), 309–326.
- Wood, D.S., Oertel, G., Singh, J., Bennett, H.F., 1976. A discussion of natural strain and geological structure - Strain and anisotropy in rocks. *Philos. Trans. R. Soc. London* 283, 27–42. <https://doi.org/10.1098/rsta.1976.0067>.
- Wright, T.O., Platt, L.B., 1982. Pressure dissolution and cleavage in the Martinsburg shale. *Am. J. Sci.* 282 (2), 122–135. <https://doi.org/10.2475/ajs.282.2.122>.
- Xue, J., 2002. A brief look at Chinese Slate. *Traditional Roofing Magazine* 2, 16–17.
- Zimak, J., Losos, Z., Novotni, P., Dobe, P., Hladkova, J., 2002. Study of vein carbonates and notes to the genesis of the hydrothermal mineralization in the Moravo-Silesian Culm. *J. Czech Geol. Soc.* 47, 111–122.